POLITECNICO DI TORINO

Master of Science in Mechanical Engineering

Master's Degree Thesis

Induction hardening simulation of crankshaft

Politecnico di Torino

Supervisor

Carlo Rosso

Supervisor at Scania

Henrik Mårtensson

Examiner/supervisor at KTH

Zuheir Barsoum

Candidate

Massimo Ambrosano

A.Y. 2024-2025

Acknowledgements

I would like to express my gratitude to my supervisor at Scania, Henrik Mårtensson, for his guidance, availability and support throughout all stages of this project. His expertise and insightful suggestions have been essential not only for the completion of this thesis but also for my personal and professional growth. Thanks to him, I had the opportunity to explore complex topics, acquire new skills and face the challenges of research with greater awareness.
I would also like to thank everyone I had the pleasure of meeting at Scania, especially within the ENMDS and TGRMSPT groups, for their kindness and openness. They showed me a relaxed yet effective way of working that values employees and fosters continuous learning, allowing everyone to give their best without feeling pressured. I especially enjoyed the internal traditions, like the Friday quizzes and the daily Fika, which, as I have come to understand, is almost like a religion for Swedes (and now for me as well).
Additionally, I am grateful to my supervisors at KTH and Politecnico, Professor Barsoum and Professor Rosso, for their support, valuable advice and patience throughout the entire duration of this project.

Passando ora alla mia lingua madre, vorrei ringraziare Alessandro, con il quale ho avuto modo di scambiare idee soprattutto durante il primo anno di magistrale. Sebbene il nostro confronto sia stato limitato, è stato per me estremamente prezioso e ha contribuito in modo significativo alla mia crescita personale e accademica.
Ringrazio i miei amici, in particolare Altare, Benna e Optic, che per me rappresentano un legame di amicizia molto importante, per i tanti momenti di allegria che abbiamo condiviso in tutti questi anni. Grazie per avermi spesso ascoltato parlare di ingegneria, anche se forse non eravate molto interessati, per la vostra sincerità e per avermi insegnato a divertirmi e a prendere tutto con più leggerezza.
Ringrazio profondamente la mia grande famiglia per l'educazione che mi ha donato e per la presenza sempre viva che mi ha accompagnato lungo tutto il percorso, senza i quali non sarei la persona che sono oggi.
Un ringraziamento sentito va a mio padre, per tutte le discussioni di ingegneria che abbiamo condiviso, per la conoscenza che mi ha trasmesso e per il supporto che mi ha offerto sempre con spontaneità.
E infine, grazie mamma, perché ci sei sempre stata. Hai ascoltato i miei problemi con pazienza, mi hai dato forza nei momenti più difficili, hai rallegrato le mie giornate e mi hai sempre incoraggiato a seguire la strada più impegnativa, certa che fosse alla mia portata. Ma, soprattutto, mi hai sempre voluto bene. Le parole non bastano per esprimere tutta la mia gratitudine per ciò che hai fatto per me, e ancora meno per

spiegarti quanto tu sia stata la persona più importante nella mia vita.

Abstract

Induction hardening is extensively employed in industries such as automotive, aerospace and heavy machinery, where components require superior mechanical properties and long-term durability. Despite its advantages, the process induces tensile residual stresses that may compromise component performance by initiating micro-cracks. Therefore, optimizing the process design is essential to achieve a balanced outcome in terms of surface hardness, residual stress distribution and fatigue resistance. Traditionally, process optimization has relied heavily on experimental trials, which are both time-consuming and costly. This highlights the need for more efficient and reliable alternative methods. However, induction hardening is inherently a complex multiphysics process, involving strong couplings between thermal, electromagnetic, phase transformation and mechanical phenomena. Additionally, several material properties exhibit significant temperature dependency, introducing non-linearities that make accurate stress prediction highly challenging. Consequently, no analytical methods currently exist that can precisely predict the outcomes of the process.

In response to the challenges faced by the Swedish heavy-duty truck manufacturer Scania, this thesis presents a comprehensive simulation model of the induction heating and cooling processes applied to the crankshaft of the 6 cylinder, 13 liter Scania Super engine. The model, developed with COMSOL Multiphysics version 6.3 and JMATPRO version 12.4, couples electromagnetic heating, transient thermal behavior, phase transformations and stress evolution to capture the full complexity of the process. The simulation provides detailed predictions of key process outcomes, including the temperature distribution at the end of induction heating, the resulting hardness profile and the residual stress field throughout the material. These results are validated against available experimental data to evaluate the model's accuracy and limitations. Finally, the thesis outlines future directions aimed at further improving the precision and predictive capability of the numerical simulation that has been developed.

Table of Contents

List of Figures

List of Tables

Chapter 1

Introduction

The ability to harden steel components was known as early as ancient Greece, but for centuries the precise physical phenomena governing the process remained a mystery. Significant advancements in understanding heat treatment emerged between the late 19^{th} and early 20^{th} centuries, largely due to the contributions of Adolf Martens, Robert Austen and E.C. Bain, scientists whose names are now associated with the martensite, austenite and bainite steel phases. They discovered that rapid cooling could induce phase transformations, notably the formation of martensite, which results in increased hardness when the cooling rate is sufficiently high. Further progress was enabled by developments in microscopy and dilatometry, allowing researchers to directly observe phase transformations [23].
Over the past century, heat treatment technology evolved considerably, leading to the industrial implementation of various hardening methods. Among these, induction hardening emerged as one of the most widely adopted surface hardening techniques. First introduced in the early 20^{th} century, its efficiency and adaptability have been greatly enhanced by technological advancements, such as the development of frequency converters and precise control systems. These innovations have contributed to its widespread industrial application.
Today induction hardening is highly valued in manufacturing due to several key advantages:

- Localized hardening. Only specific areas of the component are hardened reducing waste.
- High processing speed. The process is much faster than traditional heat treatment techniques.
- Energy efficiency. Induction heating is highly efficient because it generates heat directly inside the material through the resistive losses caused by the induced eddy currents, eliminating the need for external heat sources. This direct heating significantly reduces energy loss to the environment.
- Automation and integration. It can be fully automated and integrated into production lines.

- Reduced distortion compared to other heat treatments.
- Low operating costs.
- Good repeatability. Precise process control ensures consistent results.

These advantages are achieved by using electromagnetic induction to selectively heat specific areas of a component to austenitizing temperatures, followed by rapid quenching that transforms the surface layer into martensite, significantly increasing hardness. This localized phase transformation greatly enhances wear resistance and fatigue strength, making the process especially suitable for components exposed to cyclic loading and abrasive conditions. As a result, induction hardening is widely used in industries such as automotive, aerospace and heavy machinery, where components require enhanced mechanical properties.
A key example is the crankshaft, which converts the reciprocal motion of the pistons generated by the combustion into a rotational motion. As a result, the component experiences high bending and torsional loads during operation. Engine design trends, such as higher peak cylinder pressure and mass optimization, further contribute to this. To increase the fatigue strength of this critical component, certain radii and surfaces of the crankshaft, specifically the main and the crankpin journals shown in Figure 1.1, are induction hardened.

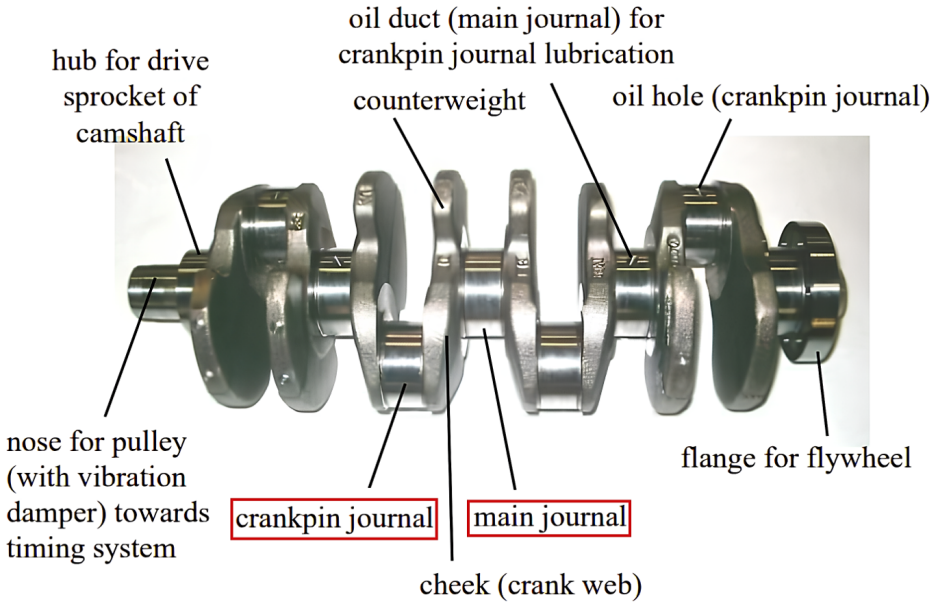

Figure 1.1: Crankshaft nomenclature with emphasis on the journals [9].

As mentioned, the process results in a locally harder material and induces compressive stresses in the martensite layer, which enhance the component's bending strength, fatigue resistance and wear resistance. However, in certain instances, high tensile stresses may develop, potentially compromising the component's service properties by leading to local micro-cracks. Additionally, excessive stresses can cause dimensional changes and distortions in the component. Therefore, it is crucial to optimize the process design to balance hardness, residual stress distribution and fatigue resistance, ensuring

optimal mechanical performance and long-term reliability.
Traditionally, optimizing induction hardening relied on experimental trials, but this approach is both time-consuming and costly; therefore, alternative approaches must be developed. However, induction hardening is a multiphysics process that involves strong couplings between various physical phenomena and the material properties exhibit strong non-linearity due to their temperature dependency. As a result, stress evolution during heat treatment is a very complicated process and there have been no analytical methods to predict it accurately [25].
Due the mentioned reasons, finite element simulations emerged in the 1970s as a powerful tool for analyzing the complex phenomena involved in heat treatment processes. This is particularly true for induction hardening, which began to be studied through simulations around 30 years ago. While simulation algorithms have become more varied and sophisticated, accurately simulating stresses and deformations remains challenging due to the need for extensive databases of thermal, metallurgical and mechanical properties of materials across the entire temperature range used during processing. Therefore, one major challenge has been the limited availability of material data required for accurate heat treatment simulations of steel. In fact, only a small portion of the necessary information is available in the open literature or within company databases.
A significant advancement came in the early 21st century with the development of softwares like JMATPRO, designed to generate material property data for heat treatment simulations. The version 12.4 of this tool has also been used to obtain material data for the current study. Additionally, modern FEM software such as ABAQUS, ANSYS, COMSOL and LS-DYNA now support thermomechanical and thermometallurgical analyses, enhancing the accuracy and feasibility of numerical simulations [11].

1.1 Aim

The present work aims to develop a detailed simulation model of the induction hardening process for the crankshaft of the 6 cylinder, 13 liter Scania Super engine of the Swedish heavy-duty truck manufacturer Scania, using the multiphysics software COMSOL version 6.3.
The primary objectives of this study are:

- Simulating the induction hardening process from both an electromagnetic and thermal perspective.
- Predicting microstructural changes and residual stress distribution in the hardened region.
- Comparing the simulation results with available experimental measurements (temperature profile, hardness distribution and residual stress measurements) to validate accuracy.

By achieving these goals, the study aims to be starting point for further fatigue analyses.

1.2 Structure of the thesis

This thesis is organized into five main chapters, each addressing a specific aspect of the research on induction hardening simulation.
Following the Introduction, which provides an overview of the heat treatment, its industrial relevance and the motivation behind developing a numerical simulation for the process, Chapter 2 State of the Art offers a comprehensive review of induction hardening. It begins with a detailed explanation of the process, followed by an discussion of the underlying physical phenomena, including electromagnetism, heat transfer, phase transformations and solid mechanics. Additionally, this chapter explores the interactions between these phenomena and their collective impact on the hardening process.
Chapter 3 Method outlines the methodology used to develop the numerical model, specifically for the sixth main journal. However, the procedure to follow for the crankpin analysis is the same. This section describes the construction of the system geometry within the simulation software and provides a detailed overview of the physics interfaces and boundary conditions for both the induction heating and cooling phases. Furthermore, it discusses the temperature-dependent material properties, meshing strategies crucial for accurately capturing the physical phenomena and the numerical procedures implemented to ensure both precision and computational efficiency.
The results of the simulation are presented in Chapter 4 Results, where key outcomes, such as temperature distribution, microstructural evolution, hardness profiles and residual stresses are analyzed. These findings are then compared with available experimental data to assess the accuracy and limitations of the simulation approach. Additionally, the results of a sensitivity analysis on the heating time are presented and discussed.
Finally, Chapter 5 Final Remarks summarizes the key insights gained from this study, highlighting potential areas for model refinement and suggesting ways to improve the accuracy and reliability of the results.
In the end, the results obtained by applying the same methodology to the sixth crankpin are presented and briefly discussed in Appendix A.

Chapter 2

State of the Art

2.1 Process description

The induction hardening process consists of two key stages: heating and quenching. During the heating phase, an alternating current flows through a coil, generating a surrounding electromagnetic field. To effectively heat the workpiece, a significant current is required to create a magnetic field strong enough for the job. As a result, power supplies must be designed to deliver extremely high output currents.
However, directly generating such high currents from a power supply can be inefficient and challenging. To address this, a resonant circuit is often used to optimize power delivery. This helps reduce the actual current or voltage requirements at the frequency converter stage, improving efficiency.
A typical resonant circuit includes components such as variable ratio transformers, capacitors and sometimes inductors. These components are connected between the power supply and the induction coil, playing a crucial role in efficient energy transfer. Their primary function is to adjust the impedance between the power supply and the induction coil, a process known as load matching.
Additionally, since the impedance of the workpiece changes as it heats up, continuous adjustment is necessary to ensure that the induction coil always receives the correct amount of power. This dynamic adjustment is vital for maintaining consistent heating and preventing energy inefficiencies throughout the process [17].
However, the electromagnetic field is affected not only by the intensity of the applied current and the material of the inductor, typically copper, due to its high electrical conductivity, but also by the coil's geometry. In the studied process, U-shaped open coils are used; however, depending on the component to be hardened, various other inductor geometries may be employed, as illustrated in Figure 2.1.

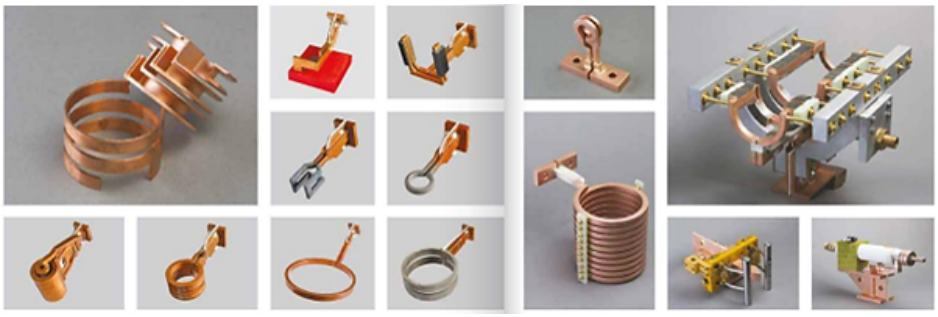

Figure 2.1: Examples of coils used for induction heating [22].

In general, open coils tend to be less efficient than ring coils, causing larger field dispersions. To mitigate this effect and improve efficiency, field concentrators (also called flux controllers, intensifiers, diverters or magnetic shunts) are typically employed. These concentrators are commonly made of ferromagnetic powder cast in a Teflon body, helping to focus the electromagnetic field more effectively thanks to the high material's permeability (Figure 2.2). Therefore, several advantages come from the employment of these components:

- Selective heating of specific areas of the workpiece is enabled.
- The electrical efficiency of the inductor is enhanced.
- Undesirable heating of nearby regions is highly reduced [19].

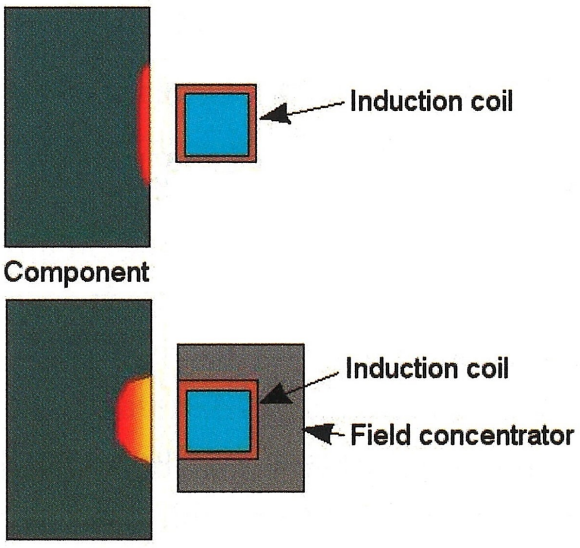

Figure 2.2: Effect of the field concentrators [23].

Regardless of the presence of field concentrators, since the conductor produces one or several loops, the magnetic flux will be concentrated inside it and the current density

will mostly flow on the inner layer of the coil. As the inductor is brought close to the crankpin and main bearing surfaces, the electromagnetic field induces eddy currents in the workpiece, as shown in Figure 2.3.

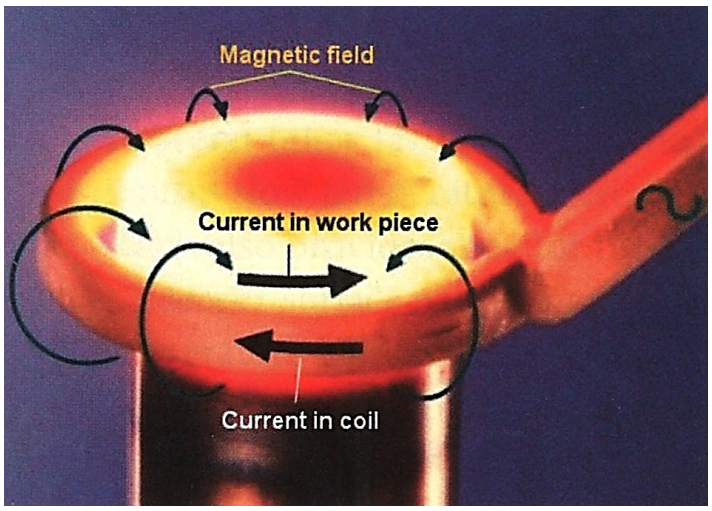

Figure 2.3: Principles of induction heating [23].

It is important to note that the induced eddy currents tend to oppose the magnetic field of the coil, resulting in a higher concentration of currents near the surface of the workpiece. This phenomenon, known as skin effect, causes the current density to decrease significantly as the distance from the surface increases, tapering off towards the core of the component. Figure 2.4 illustrates an example of the spatial variation of current density with respect to the radial distance from the surface.

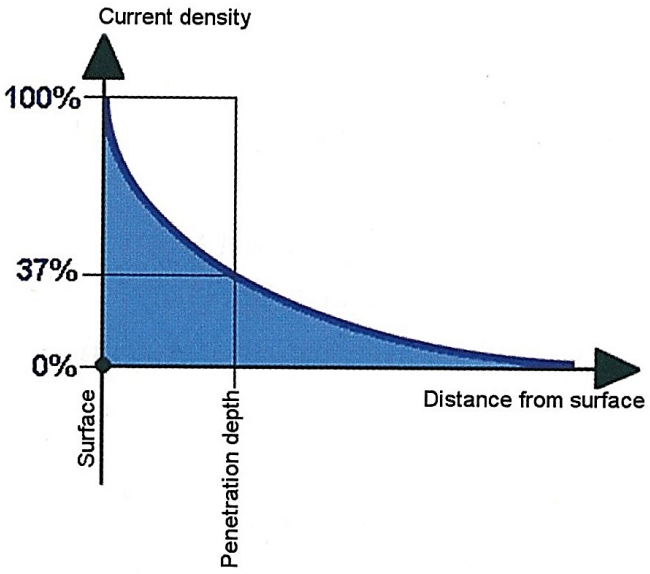

Figure 2.4: Electromagnetic penetration depth [23].

To describe this phenomenon, the electromagnetic penetration depth δ, which represents the distance from the surface at which the current density drops to 37% of its value at the surface, is introduced:

$$\delta = 503\sqrt{\frac{\rho}{\mu f}}, \tag{2.1}$$

where ρ is the material's resistivity, μ is the material's permeability and f is the current frequency. Therefore, varying the frequency directly affects the electromagnetic penetration depth, allowing for precise control over the hardening profile.
The currents induced in the workpiece then generate heat due to the electrical resistance. Therefore, while any conductive material can be hardened through induction, the process is more effective when the component has higher electrical resistance. It follows that a poor conductor, as the steel used for the crankshaft discussed in this report, will heat up more effectively than a good conductor, as the copper employed for the coil. Additionally, there is a heating effect due to hysteresis losses up to the Curie temperature (around 770°C), but this effect typically contributes less than 10% to the total heating.
The heat generated by the electromagnetic field raises the temperature of the workpiece and to achieve uniform heating using the U-shaped coil, the crankshaft must rotate around its main axis. The thermal process induces a phase transformation, where the initial body-centered-cubic (BCC) lattice structure transitions into a face-centered-cubic (FCC) lattice (Figure 2.5).

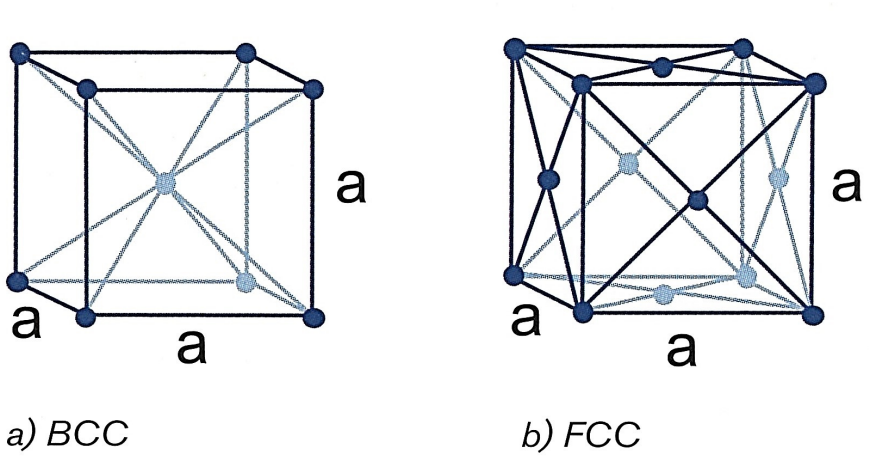

Figure 2.5: BCC and FCC lattice structures [23].

As shown in the phase diagram in Figure 2.6, the initial ferritic-pearlitic steel microstructure begins to transform into austenite once the temperature exceeds a critical threshold, denoted as A_1. This transformation occurs progressively and becomes more rapid as the temperature increases. When it surpasses the upper threshold, A_3, the steel reaches a fully austenitic microstructure. This explains why the heating process is also referred to as austenitization.

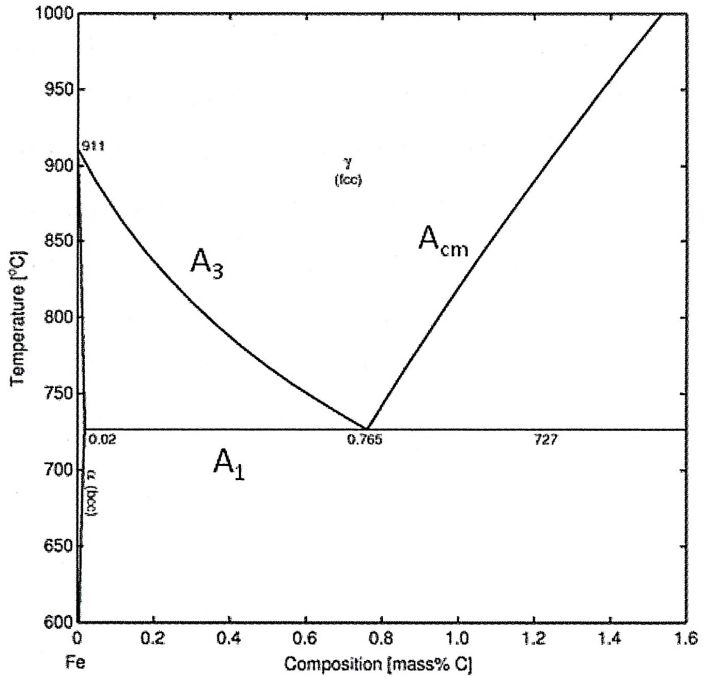

Figure 2.6: Detail of the iron-carbon phase diagram [23].

It is important to note that the time required for the process can vary depending on the alloying elements present in the material.
After the heating phase, the component undergoes rapid cooling. One of the most common methods is spray quenching, which involves applying a cooling medium, typically water, oil or polymer-based solutions, through nozzles in the form of a high velocity spray directed at the surface of the heated component (Figure 2.7).

Figure 2.7: Example of the setup for spray quenching [17].

This arrangement allows for precise control of the cooling rate, which can be adjusted by modifying the spray pressure, mass flow rate, nozzle configuration and coolant type. Moreover, unlike traditional immersion quenching, spray quenching ensures a more uniform cooling effect, reducing thermal stresses and minimizing the risk of distortion. Depending on the effective cooling rate, different phase transformations may occur (Figure 2.8).

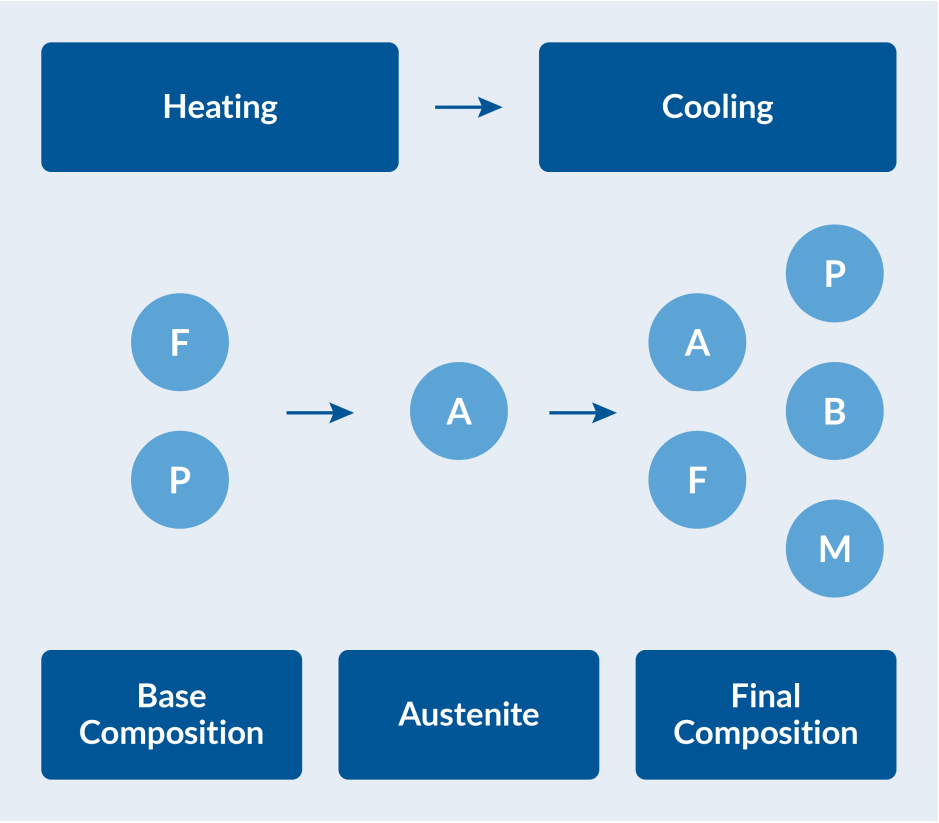

Figure 2.8: Phase composition during heating and cooling. The base composition of ferrite (F) and pearlite (P) transforms into austenite (A) on heating. The austenite can decompose into ferrite, pearlite, bainite (B) and martensite (M) during cooling [8].

The goal is to form martensite, a phase known for its high mechanical properties, through a diffusionless transformation. This process involves the deformation of the FCC austenitic crystal structure into the BCT (body-centred-tetragonal) martensitic lattice. Figure 2.9 illustrates the geometric differences among the three main phases. Specifically, it shows that the martensite lattice closely resembles that of ferrite, but is distorted due to the presence of a carbon atom. In fact, this transformation occurs only at high cooling rates because, under such conditions, the carbon atoms do not have sufficient time to diffuse out of the initial lattice structure, leaving it deformed and resulting in a metastable phase. Indeed, the carbon content plays a crucial role in determining the mechanical properties of the resulting martensitic microstructure, influencing characteristics such as hardness and wear resistance.

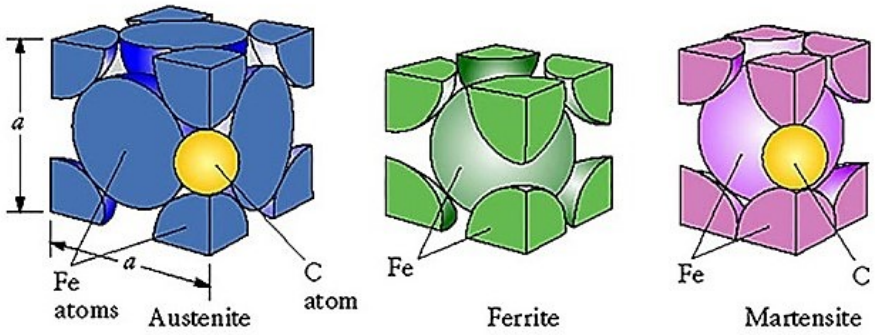

Figure 2.9: Unit cell for austenite, ferrite and martensite [7].

To visualize the cooling rates required for a diffusionless transformation, one can refer to the CCT (Continuous-Cooling-Transformation) diagram, as shown in Figure 2.10, where it is displayed an example of the different microstructures obtained for selected cooling rates.

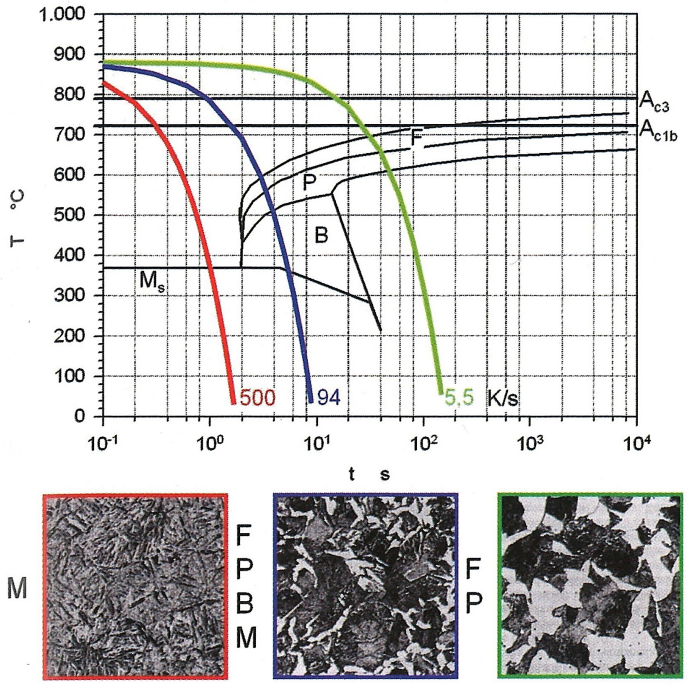

Figure 2.10: CCT diagram and microstructures produced at different cooling rates for a selected steel (F = ferrite, P = pearlite, B = Bainite, M = martensite) [23].

From the previous diagram, the critical quenching time, which represents the maximum time allowed for cooling the steel to the martensite start temperature (M_s), can be evaluated. This time ensures that the austenitized volume passes beyond the ferrite, pearlite and bainite noses. The critical quenching time depends on the alloying content and can range from just a few seconds for low-alloy steels to several minutes

for high-alloy steels. Consequently, depending on the material, the process parameters and coolant type must be carefully selected.
In the end, a small portion of the material just beneath the surface undergoes hardening, significantly enhancing its fatigue and wear resistance. This hardened region can be easily identified in a cross-sectional view of the heat treated component, where it appears as a darker material section, indicating its increased hardness, as shown in Figure 2.11.

Figure 2.11: Cross section of an induction hardened component [22].

The rapid heating and cooling cycles during heat treatment, along with the resulting phase transformations, induce residual stresses in the material. During austenitization, thermal stresses cause plastic deformation near the surface. Additionally, residual stresses develop during quenching due to spatial and temporal variations in temperature, leading to a significant thermal gradient within the material. This thermal gradient results in unequal contraction and a nonuniform microstructure. Unequal contraction generates thermal strain, while the nonuniform microstructure leads to phase transformation strain. The surface cools first, developing tensile stresses due to thermal shrinkage, while the core undergoes compression to balance the tensile at the surface. Subsequently, when the temperature reaches the martensite start point, the transformation of austenite to martensite causes compressive stresses due to volume expansion and the effects of transformation-induced-plasticity (TRIP). To maintain force equilibrium, tensile stresses are formed just below the hardened zone [21].
Figure 2.12 illustrates an example of the residual stress distribution as a function of the distance from the surface, highlighting a peak located just beneath the hardened layer. This peak originates from plastic deformation that occurs during the heating phase, leading to the development of elevated tensile stresses in this region. However, these stresses are typically reduced through the tempering process, where the workpiece is reheated to a controlled temperature range. This treatment slightly lowers the mechanical strength but significantly reduces material brittleness, enhancing overall structural integrity.

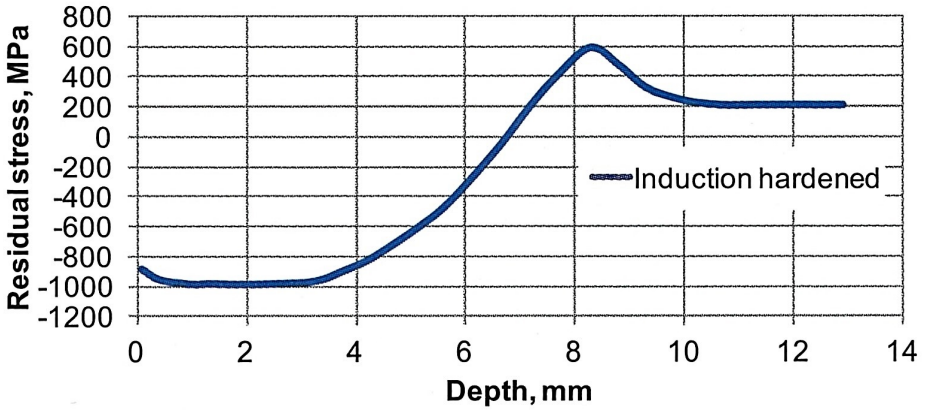

Figure 2.12: Residual stress profile for an induction hardened steel [23].

The residual stress profile shown above can be obtained by means of different methods, as x-ray, neutron or synchrotron diffraction, respectively. In particular the last two procedures are non-destructive and therefore are of particular interest [12].

2.2 Theoretical background

From the process description provided in the previous section, one can state that to model the complete induction hardening process it is necessary to consider several phenomena, namely the electromagnetic field generated by the coil, the temperature evolution in the workpiece, the phase transformations and the induced mechanical stresses. A schematic representation of the phenomena involved and their relationships is provided in Figure 2.13.

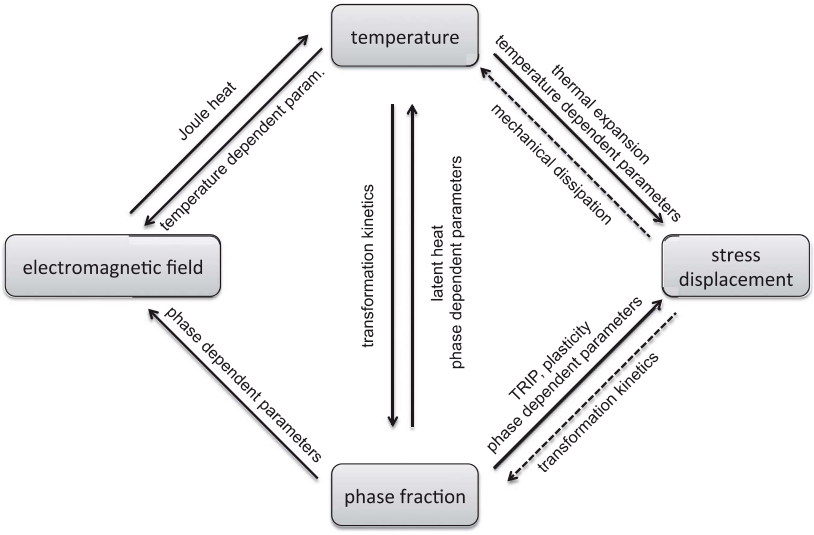

Figure 2.13: Schematic representation of the phenomena involved [13].

In the following sections, the main equations describing the phenomena shown in the figure above will be presented and discussed.

2.2.1 Electromagnetism

The electromagnetic field generated by the coil during the induction heating process is described by Maxwell's equation as follows:

$$\nabla \cdot \mathbf{D} = \rho \tag{2.2}$$

$$\nabla \cdot \mathbf{B} = 0 \tag{2.3}$$

$$\nabla \times \mathbf{E} = -\frac{\partial \mathbf{B}}{\partial t} \tag{2.4}$$

$$\nabla \times \mathbf{H} = \mathbf{J} + \frac{\partial \mathbf{D}}{\partial t}, \tag{2.5}$$

where $\mathbf{D}$ and $\mathbf{E}$ are the electric flux density and electric field intensity, while $\mathbf{J}$ represents the conduction current density. Moreover, $\mathbf{B}$ is the magnetic flux density and $\mathbf{H}$ is the magnetic field intensity.
It has to be noted that since the coil excitation current frequency is lower than 1 MHz, the displacement current $\partial \mathbf{D}/\partial t$ can be neglected, compared to the conduction current density, using a quasi-static approximation [24].
Therefore, Eq.(2.5) becomes

$$\nabla \times \mathbf{H} = \mathbf{J} \tag{2.6}$$

The relationship between these quantities and the material properties is specified below:

$$\mathbf{D} = \varepsilon_0 \varepsilon_r \mathbf{E} \tag{2.7}$$

$$\mathbf{J} = \sigma \mathbf{E} \tag{2.8}$$

$$\mathbf{B} = \mu_0 \mu_r \mathbf{H}, \tag{2.9}$$

where ε_0 is the vacuum permittivity (constant and equal to $8.854 \cdot 10^{-12}$ F/m), ε_r is the relative permittivity of the material, σ is the electrical conductivity of the material, μ_0 is the vacuum magnetic permeability (constant and equal to $1.257 \cdot 10^{-7}$ N/A^2) and μ_r is the relative permittivity of the material.
The Maxwell's equations can be simplified by introducing two additional relationships involving the magnetic vector potential $\mathbf{A}$ and the electric scalar potential φ [20]:

$$\mathbf{B} = \nabla \times \mathbf{A} \tag{2.10}$$

$$\mathbf{E} = -\frac{\partial \mathbf{A}}{\partial t} - \nabla \varphi \tag{2.11}$$

The aforementioned relations, together with the material constitutive expressions (Eq. (2.7) - (2.9)) and the application of the Coulomb gauge ($\nabla \cdot \mathbf{A} = 0$), can be substituted in the Maxwell's equations to obtain the final equations to be solved for an harmonic excitation:

$$\nabla \times \left(\frac{1}{\mu_0 \mu_r} \nabla \times \mathbf{A} \right) - \nabla \left(\frac{1}{\mu_0 \mu_r} \nabla \mathbf{A} \right) + j\omega\sigma \frac{\partial \mathbf{A}}{\partial t} + j\omega\sigma \nabla \varphi = 0 \tag{2.12}$$

$$\nabla \cdot \left(-j\omega\sigma \frac{\partial \mathbf{A}}{\partial t} - j\omega\sigma \nabla \varphi \right) = 0, \tag{2.13}$$

where j is the imaginary unit and ω is the angular frequency.

2.2.2 Heat transfer

Eddy currents derived by the electromagnetic model manifest themselves through heat production due to the Joule effect. The heat is then distributed throughout the workpiece by conduction. The process is described by the equations of heat transfer [10].

$$\rho c \frac{\partial T}{\partial t} + \rho c \, \mathbf{u} \cdot \nabla T + \nabla \cdot (\mathbf{q}) = Q \quad \text{where} \quad \mathbf{q} = -\lambda \nabla T, \tag{2.14}$$

where λ is the thermal conductivity, ρ is the density, c is the specific heat capacity, $\mathbf{u}$ is the velocity field and Q is the heat source including the effect of eddy currents, latent heat of phase transformation, convection and radiation. More in detail, the thermal power generated by the eddy currents is described by the Joule equation.

$$Q_e = \mathbf{J} \cdot \mathbf{E}, \tag{2.15}$$

while the heating power released during the transformation from a source to a destination phase is defined as

$$Q_0 = \Delta H_{s \to d} \, \dot{\xi}^d \tag{2.16}$$

Here $\Delta H_{s \to d}$ represents the enthalpy per unit volume and $\dot{\xi}^d$ denotes the rate of formation of the destination phase. Since every phase transformation can release heat, all their contributions will be added and used as a source on the right side of Eq.(2.14).
The convective heat exchange between the surface of the workpiece and the surrounding air is expressed as

$$q_c = h(T - T_a), \tag{2.17}$$

where h is the convective heat transfer coefficient and T_a is the temperature of the environment. The same mechanism is exploited to cool down the coil and the workpiece, through air and water cooling. The difference lies in the type of convection: natural for air and forced for the cooling fluid. This results in a much higher heat transfer coefficient in the second case.
In the end, when the workpiece reaches very high temperatures, heat transfer by radiation takes place. The phenomenon is governed by the Stefan-Boltzmann equation:

$$q_r = \varepsilon \sigma_s (T_s^4 - T_a^4), \tag{2.18}$$

where ε is the surface emissivity and σ_s is the Stefan-Boltzmann constant (equal to $5.57 \cdot 10^{-8} \mathrm{W/m^2K^4}$).

2.2.3 Phase transformation

As described in Section 2.1, five possible microstructures may be present. For diffusion-controlled phase transformations, such as the production of ferrite, pearlite and bainite, the process is both temperature and time dependent. It is commonly modeled using

the Johnson–Mehl–Avrami–Kolmogorov (JMAK) model [15], which is governed by the following equation:

$$\xi^d = \xi_0^d + \left(\xi_{eq}^d - \xi_0^d\right)\left(1 - \exp\left(-\left(\frac{t}{\tau_{s\to d}}\right)^{n_{s\to d}}\right)\right), \tag{2.19}$$

where the subscripts s and d represent the source and destination phases, respectively. The term ξ^d denotes the fraction of the transformed phase at time t, while ξ_0^d and ξ_{eq}^d represent the initial and equilibrium phase fractions respectively (with ξ_{eq}^d being the phase fraction as $t \to \infty$). The characteristic transformation time $\tau_{s\to d}$ depends on the transformation conditions, while the Avrami exponent $n_{s\to d}$ describes the mechanism and kinetics of the transformation. All these parameters are typically functions of temperature.
Rewriting Eq.(2.19) in the usually employed rate form, it yields:

$$\dot{\xi}^d = \frac{\xi_{eq}^d - \xi^d}{\tau_{s\to d}} n_{s\to d}\left(\ln\left(\frac{\xi_{eq}^d - \xi_0^d}{\xi_{eq}^d - \xi^d}\right)\right)^{1-\frac{1}{n_{s\to d}}} \tag{2.20}$$

where the time dependency is now implicit. From this equation, it follows that the phase transformation occurs only when $\dot{\xi}^d$ is greater than zero.
The JMAK model can be calibrated using the Time-Temperature-Transformation (TTT) diagram, which applies when the material is rapidly taken from an initial state to a specified temperature and held isothermally. This diagram typically presents different curves depending on the specified destination phase fraction (Figure 2.14), providing essential information on the time and temperature conditions required to achieve the target result.

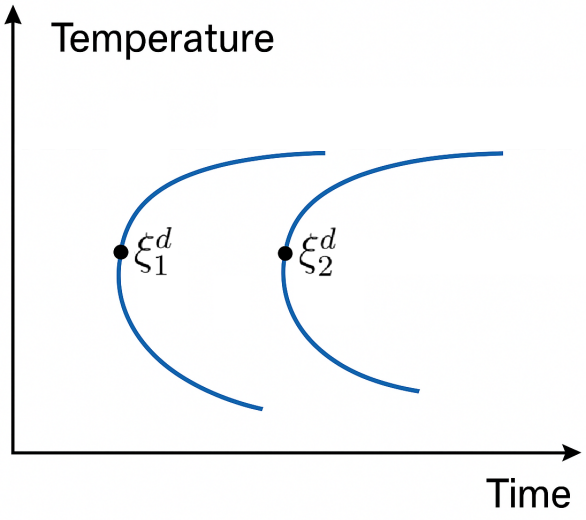

Figure 2.14: Scheme of a TTT diagram with two constant phase fraction curves [3].

In the JMAK model, two curves from the TTT diagram are needed, as the Avrami

exponent and the time constant can be determined using the following expressions:

$$n_{s\to d} = \ln\left(\frac{\ln(1-X_1)}{\ln(1-X_2)}\right) / \ln\left(\frac{t_1}{t_2}\right) \tag{2.21}$$

$$\tau_{s\to d} = t_1 / \left(-\ln(1-X_1)\right)^{\frac{1}{n_{s\to d}}}, \tag{2.22}$$

where X_1 and X_2 are the relative phase fractions, defined as

$$X_1 = \frac{\xi_1^d}{\xi_{eq}^d} \tag{2.23}$$

$$X_2 = \frac{\xi_2^d}{\xi_{eq}^d} \tag{2.24}$$

Once the two curves in the TTT diagram are selected, ξ_1^d and ξ_2^d are fixed, while the transformation times t_1 and t_2 vary with temperature.
The martensitic transformation, in contrast, is diffusionless and occurs extremely rapidly. As a result, it can be considered nearly instantaneous and independent of time. This transformation is well described by the Koistinen-Marburger equation [14], which quantifies the fraction of martensite formed as a function of undercooling below the martensite start temperature, M_s, computed starting from the weight percentage of the alloying elements using the Andrews' empirical model as follows [6]:

$$M_s = (539 - 423\mathrm{C} - 30.4\mathrm{Mn} - 12.1\mathrm{Cr} - 17.7\mathrm{Ni} - 7.5\mathrm{Mo})\ ^\circ\mathrm{C} \tag{2.25}$$

It has to be noted that above M_s, no transformation from austenite (the source phase) to martensite (the destination phase) takes place. Below this temperature, the fraction of martensite formed increases proportionally with undercooling $(M_s - T)$. In rate form, the Koistinen–Marburger equation can be expressed as:

$$\dot{\xi}^d = -\xi^s \beta \dot{T}, \tag{2.26}$$

where β is the Koistinen-Marburger parameter, frequently assumed to be around 0.011 1/K, though it can be explicitly computed using the following equation:

$$\beta = -\frac{\ln(0.1)}{M_s - M_{90}}, \tag{2.27}$$

in which M_{90} is the martensite finish temperature, where a 90% destination phase fraction is achieved.
Eq.(2.26) is more general, and from a computational standpoint it is more suitable for implementation, but its integrated form (Eq.(2.28)) is commonly found in the literature:

$$\xi^d = \xi_0^s \left(1 - \exp\left(\beta\left(M_s - T\right)\right)\right), \tag{2.28}$$

where ξ_0^s is the starting austenite phase fraction.
At the end of the quenching process, the microstructure consists of a mixture of ferrite, pearlite and martensite. To compute the overall hardness of the material, it is first necessary to evaluate the hardness of each individual phase. Equations (2.29) and

(2.30) present the method proposed by Mayner and others for estimating the Vickers hardness of the various phases based on the weight percentage of alloying elements and the cooling rate V_r [16].

$$\begin{aligned} HV^{f,p} = 42 + 223\text{C} + 53\text{Si} + 30\text{Mn} + 12.6\text{Ni} + 7\text{Cr} + 19\text{Mo} \\ + (10 - 19\text{Si} + 4\text{Ni} + 8\text{Cr} + 130\text{V}) \log(V_r) \end{aligned} \tag{2.29}$$

$$HV^m = 127 + 949\text{C} + 27\text{Si} + 11\text{Mn} + 8\text{Ni} + 16\text{Cr} + 21 \log(V_r), \tag{2.30}$$

where the hardness of ferrite and pearlite are assumed equal to each other.
The global hardness is then determined as a weighted average of the individual phases hardness, where the weights correspond to the respective phase volume fractions:

$$HV = (\xi^f + \xi^p) HV^{f,p} + \xi^m HV^m \tag{2.31}$$

2.2.4 Solid mechanics

The main governing equation for the mechanical effects is the balance of momentum:

$$\rho \frac{\partial^2 \mathbf{u}}{\partial t^2} = \nabla \cdot \mathbf{S} + \mathbf{f}_v, \tag{2.32}$$

where ρ is the density, $\mathbf{u}$ is the deformation vector, $\mathbf{S}$ is the stress tensor and $\mathbf{f}_v$ is the external volume force (such as gravity). Assuming small deformations and neglecting the effect of external volume forces, Eq.(2.32) simplifies to:

$$\nabla \cdot \mathbf{S} = 0 \tag{2.33}$$

The total strain ε, instead, can be expressed as the superposition of elastic and inelastic contributions:

$$\varepsilon = \varepsilon^{el} + \varepsilon^{inel} = \frac{1}{2} \left[\nabla \mathbf{u} + (\nabla \mathbf{u})^T \right], \tag{2.34}$$

where ε^{el} represents the elastic strain, associated with the material's linear behavior under stress. This strain is fully reversible upon unloading and it arises when deformation is proportional to the applied stress, as described by the following equation:

$$\mathbf{S}^{el} = \mathbf{C} : \varepsilon^{el}, \tag{2.35}$$

where $\mathbf{C}$ denotes the linear stiffness tensor, which is a function of Young's modulus and Poisson's ratio [4].
The term ε^{inel}, instead, accounts for inelastic strain, encompassing all permanent deformations in the material, including:

- ε^{th}: thermal strain, induced by temperature variations. Thermal expansion or contraction is particularly significant during phase transformations; for instance, the transformation from austenite to martensite involves thermal contraction due to cooling, accompanied by volumetric expansion as martensite forms.

- ε^{TRIP}: strain coming from phase transformation-induced plasticity (TRIP), a phenomenon distinct from conventional plasticity. Unlike classical plasticity, which follows a yield criterion, TRIP occurs at stress levels insufficient to induce plastic deformation even in the softer phases.
- ε^{em}: strain induced by electromagnetic forces, which is typically small compared to thermal and structural strains and can generally be neglected. These forces usually have a noticeable effect only in specific situations, such as when heating flat surfaces or long parts with thin profiles [18].

Additionally, plastic strain leads to an increase in yield stress. Assuming a linear isotropic hardening model, where the plastic deformation of the material is described by a straight line, the hardening function can be expresses as follows:

$$\sigma_y = \sigma_{y0} + E_{iso}\,\varepsilon^{pe}, \quad \text{with} \quad \varepsilon^{pe} = \sqrt{\frac{2}{3}\varepsilon^{pl} : \varepsilon^{pl}}, \tag{2.36}$$

where σ_y is the instantaneous yield stress, σ_{y0} is the initial yield stress, ε^{pe} is the equivalent plastic strain and E_{iso} is the isotropic hardening modulus, derived from

$$\frac{1}{E_{iso}} = \frac{1}{E_{Tiso}} - \frac{1}{E}, \tag{2.37}$$

in which E_{Tiso} is the isotropic tangent modulus.
The thermal strain ε^{th} computation, instead, can be based on the change in density of the different phases during the variation of temperature, or, alternatively, it can be calculated by using a phase fraction weighted sum of the thermal strain of each phase. The corresponding equation for the density-based formulation is:

$$\varepsilon^{th} = \frac{\rho}{\rho_{th}} - 1 = \frac{\sum_{i=1}^{N} \xi_0^i \rho^i(T_{ref}^i)}{\sum_{i=1}^{N} \xi^i \rho^i(T)} - 1, \tag{2.38}$$

where ρ represents the initial density, computed at a reference temperature for each phase and weighted with the phase fractions, while ρ_{th} is the evolving density.
In the strain-based formulation, instead, the total contribution to the thermal strain is given by:

$$\sum_{i=1}^{N} \xi^i \varepsilon_{th}^i, \tag{2.39}$$

where the thermal strain contribution of the different phases is computed using the secant thermal expansion model, defined by the following equation:

$$\varepsilon_{th}^i = \xi^i \alpha^i(T)(T - T_{ref}^i), \tag{2.40}$$

where $\alpha^i(T)$ and T_{ref} are the thermal expansion coefficient and the strain volume reference temperature, at which the strain is null, relative to the phase i. Figure 2.15 shows the evolution of the thermal strain as a starting phase I transforms completely into phase II according to Eq.(2.39).

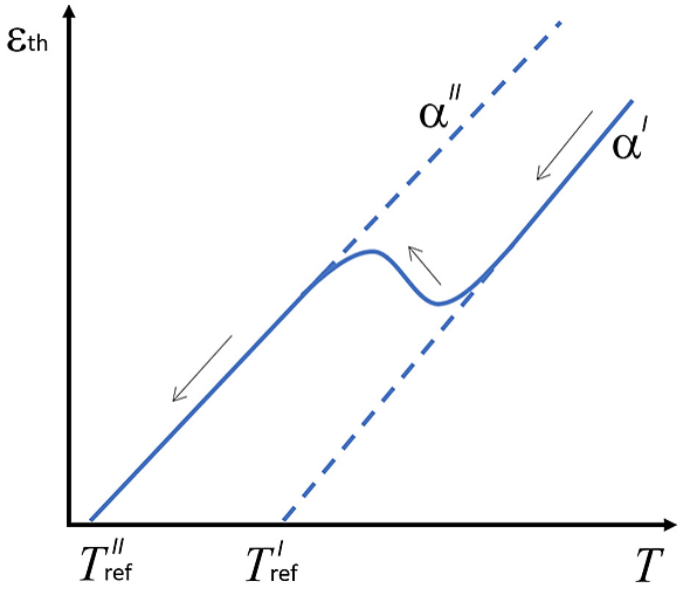

Figure 2.15: Evolution of the thermal strain according to the strain-based formulation [3].

The description of the TRIP strain is more complex, but a commonly used definition for its time derivative is:

$$\dot{\varepsilon}^{TRIP} = \frac{3}{2} K^{TRIP} \frac{d\Phi(\xi^d)}{d\xi^d} \dot{\xi}^d \cdot \mathrm{dev}(\mathbf{S}), \tag{2.41}$$

where the key parameter is K^{TRIP}, which characterizes transformation-induced plasticity and depends on several factors, such as the type of phase transformation, carbon content and temperature. A more detailed discussion of Eq.(2.41) can be found in Ref. [15].
Having defined the strain components, Hooke's law allows us to express the stress as:

$$\mathbf{S}^{el} = \mathbf{C} : (\varepsilon - \varepsilon^{inel}), \tag{2.42}$$

which is the main equation solved by the program to obtain the stress distribution.

Chapter 3

Method

3.1 Induction heating

The induction heating analysis represents the initial step in the study of the induction hardening process. It has been carried out with the finite element solver COMSOL Multiphysics version 6.3 on a full 3D model, as the lack of perfect symmetry prevents the use of geometric simplifications. This section outlines the model geometry, the employed physics interfaces, the process parameters and the material properties of the various components involved.

3.1.1 Geometry

Figure 3.1 shows the 3D model of the coil with the flux concentrators and the crankshaft journal, specifically the sixth main bearing, used for the induction heating analysis.

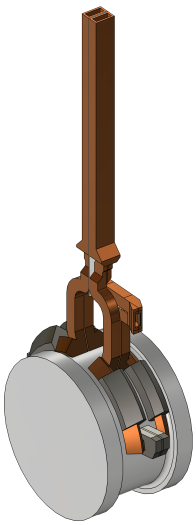

Figure 3.1: 3D model of the sixth main bearing and inductor with flux concentrators.

Compared to the real component, certain simplifications have been applied to the coil geometry. For example, the two top plates used for electric excitation have been removed, along with the cooling fluid pipe. These modifications do not affect the accuracy of the electromagnetic field modeling but serve to reduce the overall complexity of the model.
All the components are then enclosed within an air cube large enough to fully capture the electromagnetic field generated by the coil. The complete geometry analyzed in the induction heating analysis is illustrated in Figure 3.2.

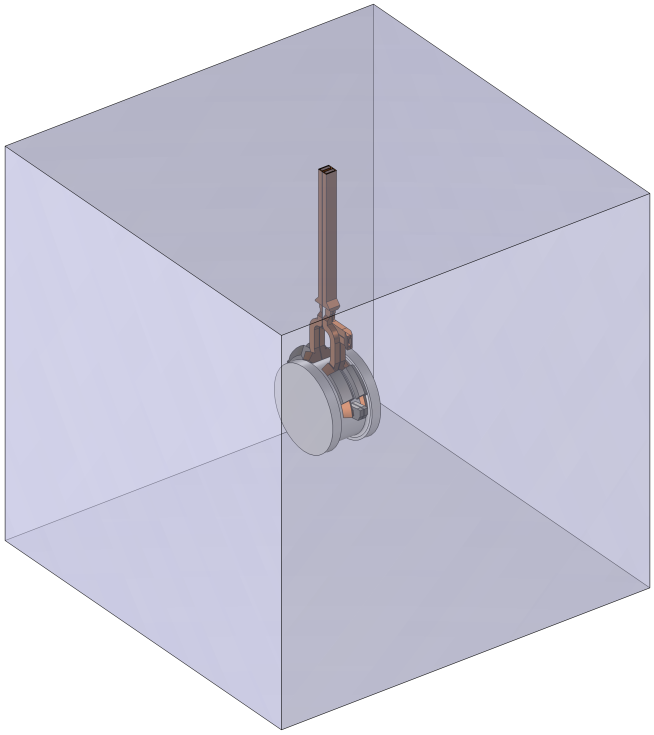

Figure 3.2: Complete 3D model employed for the induction heating analysis.

3.1.2 Physics interfaces

For accurate modeling of the induction heating process in COMSOL, three physics interfaces have been selected:

- Magnetic Fields (mf).
- Heat Transfer in Solids (ht).
- Electromagnetic Heating (emh).

As shown in the previous list, no physics interface has been employed to directly model the microstructural changes occurring during the heating phase. Instead, to simplify the model, global material properties have been generated using the software JMATPRO version 12.4.

A schematic representation of the physics interfaces selected for the induction heating simulation and the nodes employed to accurately simulate the process is shown in Figure 3.3. The detailed description of the COMSOL interfaces, along with the applied initial and boundary conditions, is provided in the following sections.

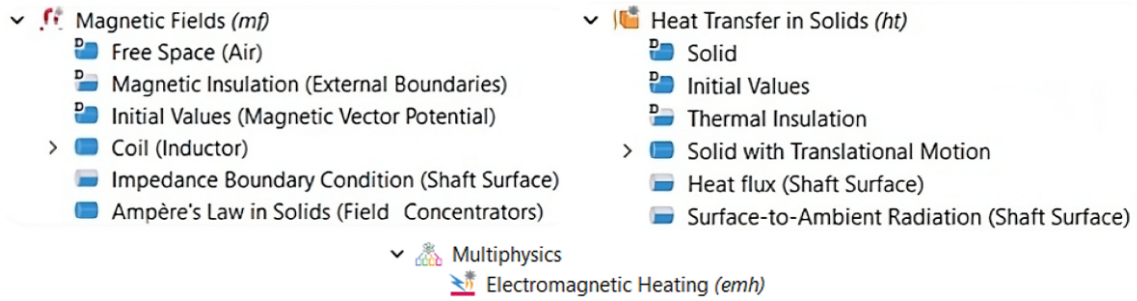

Figure 3.3: Physics interfaces selected for the induction heating simulation.

Magnetic Fields

The Magnetic Fields interface have been used to compute magnetic fields and current distributions in and around coil and workpiece. This physics interface solves Maxwell's equations, formulated using the magnetic vector potential [1]. When this module is employed, the following default nodes are added to the Model Builder:

- **Free Space**. This condition introduces the equation for the magnetic vector potential and assumes that all domains have a uniform relative magnetic permeability and permittivity of one. The conductivity is automatically determined to a value that enhances numerical stability. In fact, for transient and frequency-domain modeling of inductive devices, it is important to limit the contrast in conductivity, even though, in reality, the values can vary between $10^{-14}\,\mathrm{S/m}$ (dry air) and $6 \cdot 10^{7}\,\mathrm{S/m}$ (for copper).
- **Magnetic Insulation**. This boundary condition sets the normal component of the magnetic potential to zero at the boundary, as expressed by $\mathbf{n} \times \mathbf{A} = 0$. It is applied on the outer surfaces (of the air domain) to simulate an ideal boundary that prevents magnetic flux from crossing. In fact, while the environment surrounding the electromagnetic source is infinite in reality, in simulations, a finite domain must be defined. If the air domain is sufficiently large, the magnetic field at the boundary becomes weak and nearly parallel to the surface. Therefore, the Magnetic Insulation condition provides a good approximation for this situation, as it prevents magnetic field lines from escaping. This simplifies the problem by introducing a well defined mathematical boundary and avoids artificial influences from the domain's edges. An alternative boundary condition is the Perfect Magnetic Conductor, which sets the tangential component of the magnetic field (and consequently the surface current density) to zero. It can be shown that for sufficiently large domains, the Magnetic Insulation and the Perfect Magnetic Conductor conditions are equivalent.

- **Initial Values**. This condition assigns an initial value to the magnetic vector potential **A**, which can be used as the starting point for a transient simulation or as an initial guess for a nonlinear solver. The default value employed in this simulation is 0 Wb/m.

The Free Space condition has been maintained just for the air domain, while for other components it has been overridden by the following boundary conditions:

- **Coil**. This feature can be used to model coils, cables and other conductors subject to a lumped excitation, such as an externally applied current or voltage. In this case, the excitation consists of an alternating current with a magnitude of 7.1 kA and a frequency of 9.1 kHz. The Coil feature then converts this lumped excitation into local quantities, such as electric field and current density, and computes lumped parameters of interest, including impedance and inductance. The Coil node supports three different conductor models:

  1. *Single conductor*, which represents a single conductive body where current flows freely due to the material's conductivity. It is useful when the current flow has a well defined starting and ending point or forms a closed loop.
  2. *Homogenized multiturn*, which models a bundle of electrically thin wires tightly wound together but separated by an electrical insulator. In this case, the current flows only along the wires.
  3. *Homogenized litz*, a variant of the multiturn model, which accounts for the effects of helical twisting and multiple strands per turn.

  As discussed in Section 2, the coil used in the induction hardening studies is a single conductor with a U-shape. Therefore, the Single conductor model should be applied in this case.
  Additionally, the type of coil, defined by its geometry, has to be selected. Since in this case the coil is not circular or linear, the numeric coil type has been applied. This selection introduces the Geometry Analysis subnode, which requires the user to define the input and output surfaces for excitation, highlighted in blue in Figure 3.4.

Figure 3.4: Input (left) and Output (right) surfaces of the coil electric excitation.

- **Impedance Boundary Condition**. This condition have been applied to exterior boundaries representing the surface of a lossy component, such as the shaft. It approximates the penetration of the electromagnetic field, allowing the model to avoid the inclusion of another domain and significantly reducing computational time. However, the impedance boundary condition is a valid approximation only when the skin depth is small relative to the size of the conductor, as is the case here. The skin depth is defined as follows

$$\delta = \sqrt{\frac{2}{2\pi f \mu_0 \mu_r \sigma}} \tag{3.1}$$

  Therefore it is dependent on process parameters and material properties, which vary with the temperature.
  The alternative to this condition is to use the Ampère's Law in Solids node, which solves the electromagnetic equations also within the shaft, accounting for the field behavior inside the conductor, but increasing the model complexity.

- **Ampère's Law in Solids**. This node has been employed for modeling flux concentrators and, similar to the Free Space condition, it introduces the magnetic vector potential equation. However, it requires the specification of electromagnetic material properties, including magnetic permeability, electrical conductivity and electric permittivity.

Heat Transfer in Solids

The heat transfer equations have been solved only in the crankshaft, neglecting temperature changes in the surrounding air and the coil. This simplification is considered reasonable, given the short duration of the process and the fact that the coil temperature is maintained below 30°C by the cooling water circulating within it.
The selected physics interface, Heat Transfer in Solids, models heat transfer in solids through conduction, convection and radiation. It can also account for heat flux caused by translational motion in solids (such as the rotation of a shaft) [2]. When this version of the Heat Transfer physics interface is introduced, the following default nodes are added to the component:

- **Solid**. This node uses the heat equation (Eq.(2.14)) to model heat transfer in solids. In particular, the velocity field can be specified by adding a moving mesh node, which also captures the possible deformation of the component.

- **Thermal Insulation**. It has been applied on the external boundaries of the crankshaft and it states that the normal heat flux across the surface is null, imposing the following equation:

$$\mathbf{n} \cdot \mathbf{q} = 0 \tag{3.2}$$

- **Initial Values**. It fixes an initial value for the temperature that can serve as an initial condition for a transient simulation. For the model discussed in the present report, the initial temperature value has been set to 20 °C.

To capture the key phenomena during induction heating, the following conditions have been introduced:

- **Solid with Translational Motion**. It uses the same equation employed by the the Solid node, but it does not require the addition of a moving mesh. Instead, it needs the specification of the velocity field, which, for a component that is rotating about the z-axis, is described by the following expression:

$$\mathbf{u} = \begin{pmatrix} -\omega y \\ \omega x \\ 0 \end{pmatrix}, \tag{3.3}$$

  Here, ω represents the rotational speed required to achieve a uniform temperature distribution in the circumferential direction and it has been set to a high value of 60 rad/s to ensure this objective is met.
  This simplified condition introduces an advective contribution to the heat transfer equation and it can be applied because the simulation does not aim at considering the shaft deformation and as a result the complexity of the model is reduced by a major extent, drastically decreasing the computational time.

- **Heat Flux**. It has been applied as a boundary condition on the crankshaft surface, overriding the default thermal insulation. This node is essential for capturing the convective heat transfer between the rotating crankshaft and the surrounding air. As the crankshaft rotates, heat is transferred from the shaft to the air due to natural convection. Therefore, the Convective Heat Flux type has to be selected from the available options. A heat transfer coefficient of 5 W/m^2K has been applied, which is a typical value for natural convection of air around a cylinder.

- **Surface-to-Ambient Radiation**. Similar to the previous boundary condition, the surface-to-ambient radiation has been applied to the crankshaft surface and accounts for the heat lost due radiation to the surrounding environment. This condition requires the specification of the surface emissivity, denoted as ε, in this case set to the experimental value of 0.9.

Electromagnetic Heating

The Electromagnetic Heating coupling combines the Heat Transfer in Solids and Magnetic Fields interfaces. This physics accounts for electromagnetic losses by introducing a boundary heat source in the Heat Transfer interface according to Eq.(2.15), while also considering the temperature dependence of material properties within the Magnetic Fields interface.

3.1.3 Process parameters

The main parameters adopted in the induction heating analysis and mentioned in the discussion about the physics interfaces are summarized in Table 3.1. The frequency and

heating duration are specified by the supplier based on the particular journal requiring hardening. Similarly, the coil current magnitude depends on the specific component. However, the supplier only provides the value at the transformer input, which is not included in the simulation model. Therefore, it has been necessary to tune this parameter manually, while keeping the frequency and process duration fixed, in order to obtain a realistic surface temperature profile and thickness of the austenitic layer. Instead, the heat transfer coefficient for natural air convection, the shaft's emissivity, the ambient temperature and the initial temperature have been selected based on established industrial practices. Lastly, the rotational speed, which governs the advective heat transfer contribution, has been calibrated to ensure a uniform surface temperature distribution.

Parameter	**Value**	**Comment**
I_{coil}	7.1 kA	Electric current supplied to the coil
f	9.1 kHz	Frequency of the coil current
ω	60 rad/s	Rotational speed to induce the advective heat transfer
h_{air}	5 W/m^{2}K	Heat transfer coefficient for air natural convection
ε_{shaft}	0.9	Emissivity of the shaft surface
t_a	20 °C	Ambient temperature
t_i	20 °C	Initial temperature of the shaft
t_h	18 s	Duration of the heating process

Table 3.1: Process parameters for the induction heating simulation.

3.1.4 Material properties

Since the induction heating analysis does not aim to model microstructural changes, a global behavior has been adopted. The material used for the crankshaft journal is 48MnVS6, a high-strength steel alloy widely employed in automotive and heavy machinery components. It features a combination of different alloying elements, whose respective weight percentages and primary effects are listed in Table 3.2.

Element	**Weight %**	**Effect**
Carbon (C)	0.38	Increases hardness and strength
Manganese (Mn)	1.40	Enhances hardenability and toughness
Chromium (Cr)	0.15	Improves corrosion resistance and hardenability
Molybdenum (Mo)	0.04	Enhances high-temperature strength
Phosphorus (P)	0.013	Prevents brittleness
Silicon (Si)	0.48	Improves strength and oxidation resistance
Vanadium (V)	0.14	Increases strength and wear resistance

Table 3.2: Weight percentage of the alloying elements in 48MnVS6 and their effect.

The composition is specifically designed to improve both hardenability and strength, making the material suitable to sustain high mechanical stress and fatigue loads.
The previously discussed chemical composition determines the material properties required for the present simulation. These properties, generated using JMATPRO, are presented as functions of temperature in the following figures.

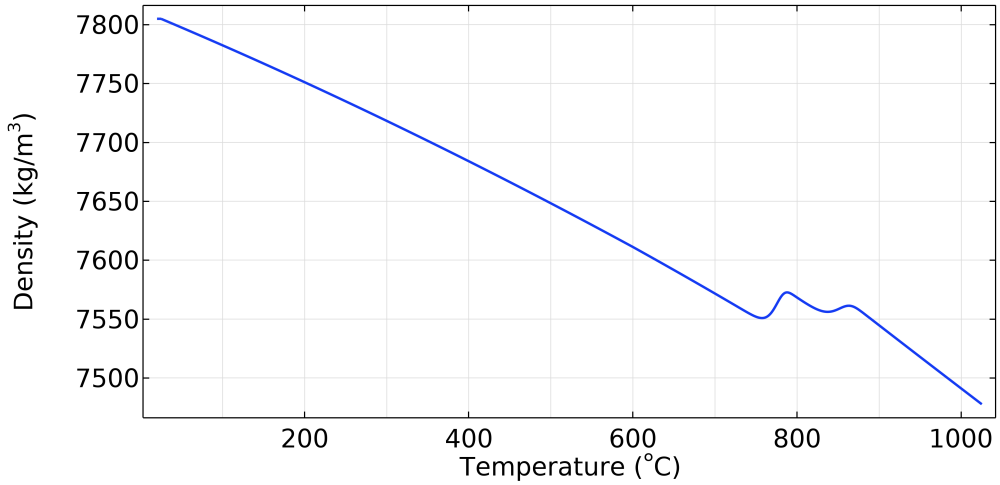

Figure 3.5: Density of 48MnVS6 as a function of temperature.

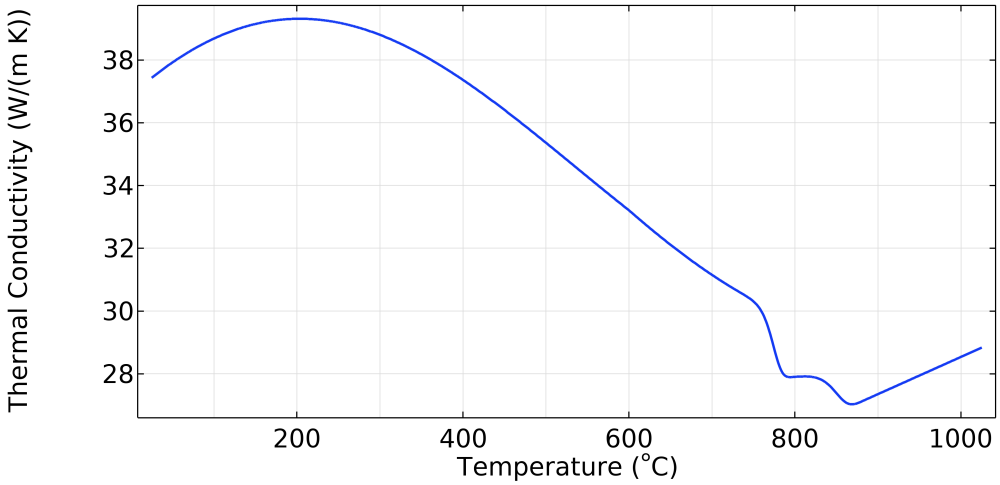

Figure 3.6: Thermal conductivity of 48MnVS6 as a function of temperature.

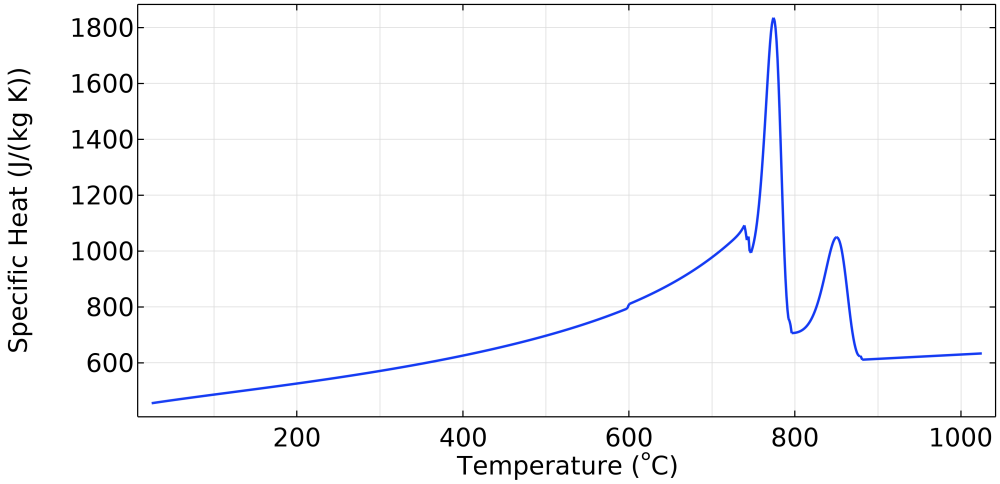

Figure 3.7: Specific heat capacity of 48MnVS6 as a function of temperature.

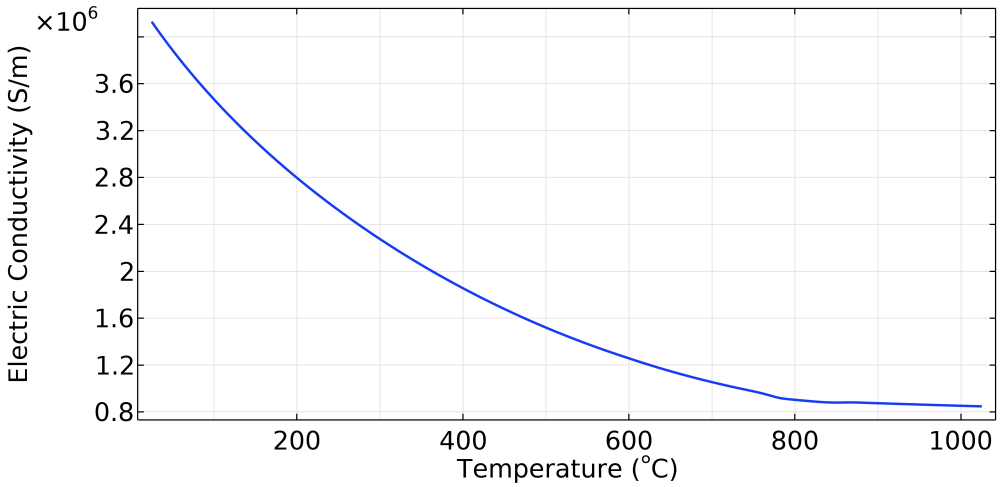

Figure 3.8: Electrical conductivity of 48MnVS6 as a function of temperature.

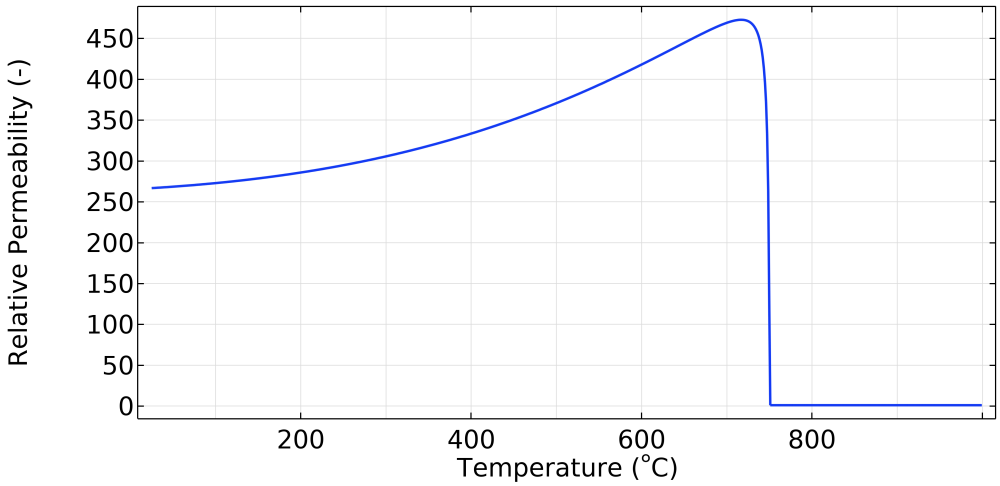

Figure 3.9: Relative permeability of 48MnVS6 as a function of temperature.

The relative permittivity plot is not shown, as it has been assumed to be temperature-independent and equal to 1.
In addition to material properties, JMATPRO has been used to obtain temperature dependent phase fraction functions for the metallurgical phases that may be present during the heating process. As shown in Figure 3.10, at room temperature the microstructure is approximately evenly divided between ferrite and pearlite. As the temperature increases, these phases gradually transform into austenite.

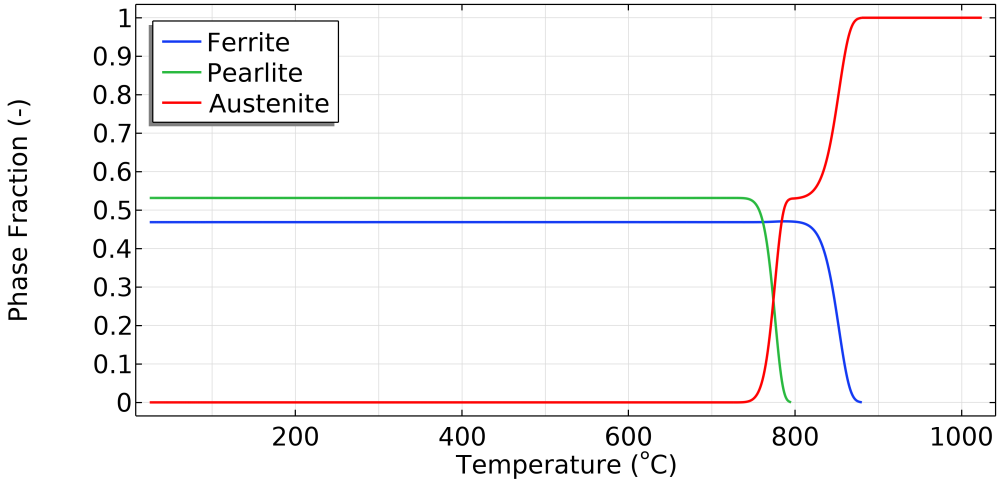

Figure 3.10: Phase fractions trend as function of temperature.

The remaining materials used in the simulation are listed below:

- **Copper**, used for the coil. It is characterized by high electrical conductivity and low magnetic permeability, which justifies the need for flux concentrators.
- **Electrical steel**, employed for the flux concentrators. It is assumed to have high magnetic permeability, which helps mitigate magnetic field dispersion, and low electrical conductivity, as these components are typically laminated to reduce eddy currents.
- **Air**, which, due to the Free Space condition discussed in Section 3.1.2, has software-defined properties.

For all these materials, the properties have been assumed to be temperature-independent and their values are reported in Table 3.3. It is important to note that, since the heat transfer equations have been solved exclusively for the crankshaft, for the other components only the electromagnetic properties need to be defined, as thermal effects are not considered.

Material	Electrical Conductivity	Permeability	Permittivity
Copper	$6{\cdot}10^7$ S/m	1	1
Electrical steel	1 S/m	1	1
Air	1-10 S/m	1	1

Table 3.3: Material properties of copper, electrical steel and air.

3.1.5 Mesh

For the induction heating study, different mesh densities have been employed to balance accuracy and computational cost. In particular, as shown in Figure 3.11, a very fine triangular mesh has been applied to the surface of the shaft to accurately capture the eddy currents computed via the Impedance Boundary Condition and the resulting heating effects.

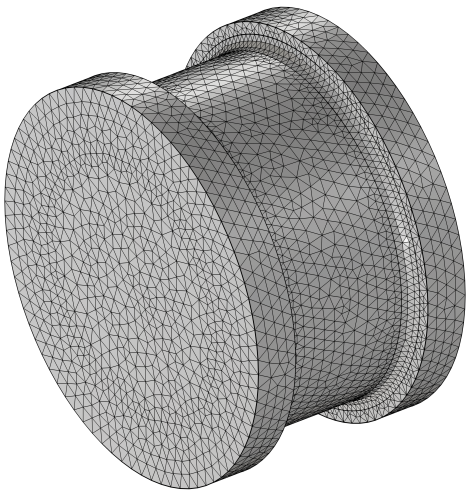

Figure 3.11: Mesh adopted for the shaft surface during heating.

For comparison, the applied mesh has a maximum element size approximately two times smaller than the one used in the predefined "extremely fine" mesh setting: 5 mm versus 12 mm. This local refinement is essential for accurately modeling the significant temperature gradients near the surface.
Throughout the rest of the domain, where the physical gradients are less pronounced, a predefined "normal" tetrahedral mesh has been used. This mesh provides a good approximation while keeping the overall number of elements within manageable limits. To highlight the difference, Figure 3.12 shows the variation in mesh density between the coil and the shaft.

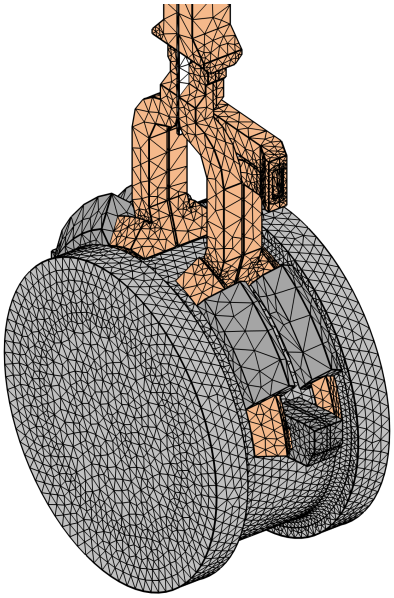

Figure 3.12: Comparison of the mesh densities applied to the coil and the shaft.

3.1.6 Simulation procedure

The induction heating analysis comprises two main study steps. The first, referred to as Coil Geometry Analysis, serves as a preprocessing stage and must be solved prior to the main electromagnetic–thermal coupling study. This step is essential for accurately determining the local direction of current flow within the coil domain, based on the prescribed input and output boundaries of the inductor.
This approach is particularly important when dealing with non-trivial coil geometries, such as the one employed in the present simulation, where the assumption of a uniform current direction would lead to significant inaccuracies in the predicted electromagnetic field distribution. By solving this initial step independently, COMSOL allows the current direction field to be precomputed and used as input for the subsequent electromagnetic analysis. This enhances both the accuracy and numerical stability of the computed magnetic field, eddy current distribution and, ultimately, Joule heating that drives the induction process.
The second study step, titled Frequency-Transient, constitutes the core of the induction heating simulation. In this phase, a frequency-domain electromagnetic analysis is performed at each time step of a transient thermal simulation.
It is important to highlight that the coupling between the Magnetic Fields and Heat Transfer in Solids interfaces is bidirectional. The electromagnetic problem defines a heat source via Joule heating, while the thermal problem updates temperature-dependent material properties, such as electrical conductivity and magnetic permeability at every time step. This mutual dependence ensures that the simulation reflects the dynamic behavior of the material as it heats up.
To solve the multiphysics problem, a Fully Coupled solver has been chosen over a Segregated one. The fully coupled approach assembles and solves a single system of equations that simultaneously accounts for all the unknown fields and their interac-

tions. This means that all multiphysics couplings are resolved within each iteration of the solver. This method is particularly advantageous when strong couplings exist between the physical phenomena, as in induction heating, where temperature-dependent material properties directly influence the electromagnetic response. By incorporating all coupling terms at once, the fully coupled approach tends to provide greater numerical robustness and typically requires fewer iterations to converge compared to the segregated strategy. However, it is important to note that each iteration of the fully coupled solver demands greater computational resources, both in terms of memory usage and processing time. Despite this, the improved convergence behavior and stability justify the additional computational cost.
Regardless of whether the Fully Coupled or Segregated approach is used, a linearized system of equations is solved at each iteration. There are two primary types of algorithms available for solving these linear systems: Direct and Iterative solvers.
Direct solvers are known for their robustness and general applicability, as they can solve large and complex systems. However, they come with significant drawbacks, primarily their high memory consumption and computational cost. As the problem size increases, both memory usage and solution time grow rapidly, which can become a limiting factor for large-scale simulations.
In contrast, Iterative solvers are more memory-efficient and require less computational time, especially for large problems. Their performance scales better with increasing model size, making them ideal for very large systems. However, Iterative solvers tend to be less robust than direct solvers and may experience slower convergence, or even fail to converge, in certain cases [5].
In this study, robust convergence has been prioritized over computational efficiency, and as a result, the Direct solver has been employed.

3.2 Cooling

The cooling analysis represents the subsequent step in the simulation of the induction hardening process. After the component is heated, it undergoes rapid cooling, or quenching, to promote the formation of martensite. This is followed by a slower cooling phase to room temperature, which facilitates the relaxation of temperature gradients and allows for the evaluation of residual stresses.
This phase of the study has been conducted using a 2D axisymmetric model, as the geometry of the crankshaft journal permits this simplification. To ensure continuity between the heating and cooling simulations, the final temperature field obtained from the 3D heating study was transferred to the 2D model. This has been achieved using a General Extrusion operator, which enables the mapping of a cross-section of the 3D temperature distribution onto the 2D domain. In fact, this operator makes it possible to determine the correspondence between points in the source and destination entities. As such, it is essential for accurately transferring data between geometries of different dimensionalities and for defining realistic initial conditions for the cooling simulation.
This section presents the cooling model in detail, including the employed physics interfaces, cooling parameters and the material properties that govern heat transfer, phase transformations and the development of residual stresses during the process.

3.2.1 Geometry

The only component subjected to cooling is the crankshaft journal. Due to the axial symmetry, a cross-sectional representation of the component can be used (Figure 3.13), significantly reducing the geometrical complexity of the model.

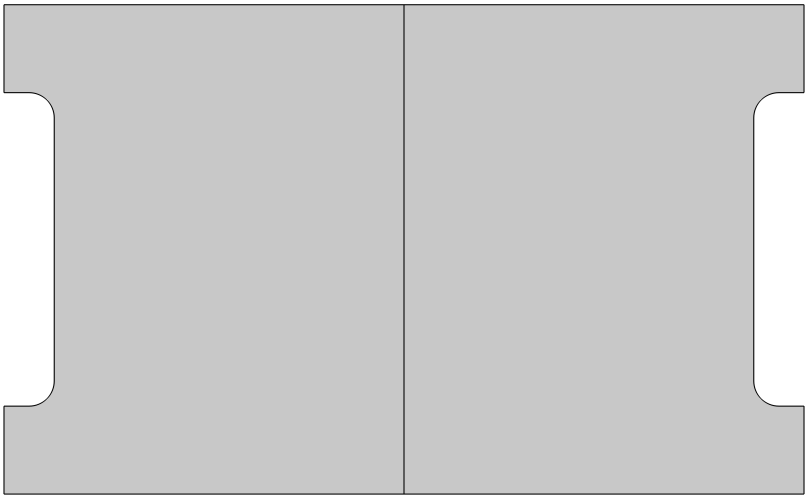

Figure 3.13: Cross-section of the crankshaft journal.

By analyzing the geometry shown in Figure 3.13, further simplification is possible by once again exploiting symmetry, resulting in just a quarter-section of the journal (Figure 3.14).

Figure 3.14: Quarter of the crankshaft journal cross-section.

3.2.2 Physics interfaces

The cooling stage requires five physics interfaces in order to capture the microstructural changes and the residual stresses:

- Heat Transfer in Solids (ht).
- Austenite Decomposition (audc).
- Solid Mechanics (solid).
- Phase Transformation Latent Heat (lht).
- Phase Transformation Strain (ptstr).

A schematic representation of the physics interfaces selected for the cooling simulation and the nodes employed to accurately simulate the process is shown in Figure 3.15. The detailed description of the COMSOL interfaces, along with the applied initial and boundary conditions, is provided in the following sections.

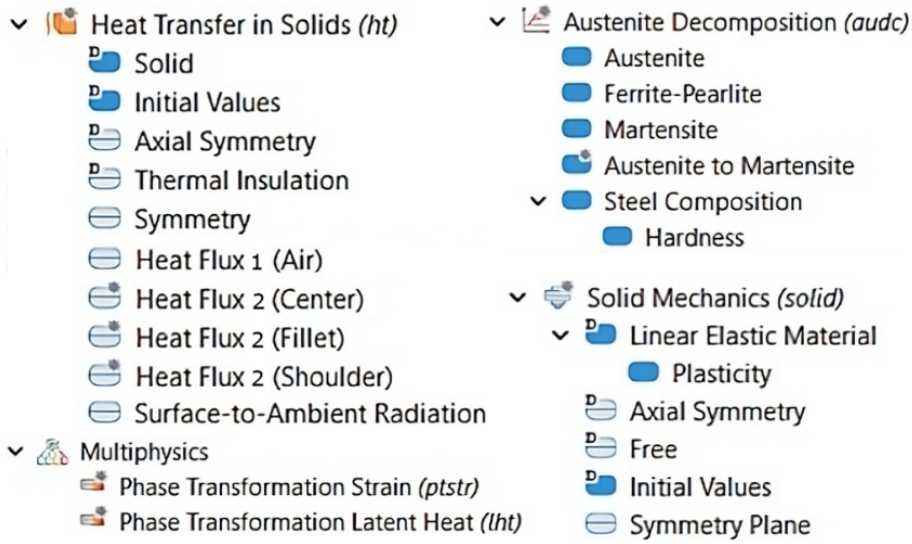

Figure 3.15: Physics interfaces selected for the cooling simulation.

Heat Transfer in Solids

The heat transfer interface employed for the cooling analysis is the same as the one used for the induction heating study. Therefore, the same default conditions have been applied by the software: Solid, Initial Values and Thermal Insulation. Additionally, since the model to be solved is axisymmetric, the Axial Symmetry boundary condition has been automatically applied on the edge highlighted in blue in Figure 3.16.

Figure 3.16: Edge where the Axial Symmetry condition has been applied.

This condition assumes that physical quantities, such as temperature, are invariant along the angular direction. Additionally, it imposes that the normal component of the heat flux is zero at the applied boundary.
Besides the default nodes, four additional conditions have been added, some of which overlaps the ones applied in the previous simulation.

- **Symmetry**. It fixes the normal heat flux equal to zero at the edge of application (Figure 3.17).
- **Heat Flux 1**. It has been applied on the whole surface, but the symmetric boundaries (Figure 3.18) and it captures the convective heat transfer between the shaft and the surrounding air throughout the whole cooling analysis. As in the heating study, the heat transfer coefficient has been set equal to 5 W/m^2K.
- **Heat Flux 2**. This condition has been applied exclusively during the quenching process to the regions targeted for hardening, as illustrated in Figure 3.19. To accurately represent the spray cooling effect, three distinct heat transfer coefficients have been assigned to the edges identified in the figure, namely the middle portion of the journal, the fillet and the shoulder. These coefficients have been calibrated to ensure that the resulting average surface temperature profiles match the experimental measurements.
- **Surface-to-Ambient Radiation**. It has been applied on the same boundaries as the previous condition and it is also active during the whole analysis. The surface emissivity is kept equal to 0.9, as in the heating study.

Figure 3.17: Edge where the Symmetry condition has been applied.

Figure 3.18: Edges where the Heat Flux 1 condition has been applied.

Figure 3.19: Edges where the Heat Flux 2 condition has been applied.

Austenite Decomposition

The Austenite Decomposition interface (audc) is designed for studying metallurgical phase transformations. This interface can compute physical effects such as the latent heat of phase transformation and transformation strains, which can be coupled with Heat Transfer in Solids and Solid Mechanics [3]. When this module is employed, several nodes are added to the model to account for the five possible microstructures (austenite, ferrite, pearlite, bainite and martensite) as well as the phase transformations involving austenite. However, in the present simulation, only the austenite-to-martensite phase transformation has been considered. Consequently, no ferrite, pearlite and bainite will form during quenching.
As a result, the only default nodes retained in the model are the following:

- Austenite
- Ferrite-Pearlite
- Martensite
- Austenite to Martensite

The metallurgical phases need the definition of the initial phase fraction, taken from the last step of the induction heating simulation, and the material properties, imported from JMATPRO.
The Austenite to Martensite node, instead, requires the selection of the transformation model, which, as specified in Section 2.2.3, is the Koistinen-Marburger model. Therefore, only two parameters need to be specified, namely the Koistinen-Marburger coefficient and the martensite start temperature. It should be noted that this node will only be active during the quenching stage, thereby preventing the formation of new martensite during the final cooling phase.
In addition to the default functionalities, the Steel Composition node has been employed to specify the chemical composition of the material in terms of weight percentage of the different alloying elements, needed to compute the martensite start temperature. Finally, the Hardness subnode has been added in order to compute the Vickers hardness of the different phases.
In the end, it is necessary to activate the various stress contributions involved in the process, namely thermal stress, phase plasticity and transformation-induced plasticity (TRIP). As discussed in Section 2.2.4, the computation of thermal stresses can be formulated based either on changes in density or on strain. In the present simulation, the strain-based formulation has been adopted and calibrated using dilatometric curves obtained from JMATPRO, allowing the identification of the reference temperatures at which each phase is considered strain-free.

Solid Mechanics

The Solid Mechanics interface has been used to solve the equations of motion and account for thermal and phase transformation stresses.

When this module is employed, the following default conditions are applied to the model:

- **Linear Elastic Material**. Applied to the entire domain, this setting introduces the governing equations for a linear elastic solid, allowing the material to deform under load according to Hooke's law.
- **Axial Symmetry**. Applied to the edge shown in Figure 3.16, this boundary condition enforces symmetry about the axis of revolution. It assumes that the displacement is independent of the azimuthal direction and restricts any displacement in the radial direction.
- **Free**. Automatically applied to all boundaries except the axis of symmetry. This condition imposes no constraints on the displacement, allowing the structure to deform freely in response to internal stresses or external loads.
- **Initial Values**. It has been used to specify the initial conditions for the displacement and velocity fields. In this case both have been set to zero.

In addition to the default conditions, two additional specifications have been introduced to exploit symmetry and account for the material's plastic deformation. The first condition, simply named Symmetry, have been applied to the same edge where the analogous Heat Transfer condition has been defined (Figure 3.17). It restricts displacement along the z-axis, effectively enforcing symmetry across that boundary.
The second specification, defined through the Plasticity node, enables the modeling of the material's hardening behavior. In this case, the hardening is described by a linear law, as expressed in Equation (2.36).
In the end, it is possible to account for the inertial terms but, despite the quenching process being time dependent, from a structural mechanics point of view, it is quasi-static and modeled as such.

Phase Transformation Latent Heat

The Phase Transformation Latent Heat multiphysics coupling introduces a volumetric heat source term into the heat equation of the coupled Heat Transfer in Solids interface, as defined by Eq.(2.16), and it is active only when enabled in the Austenite Decomposition interface. This heat source accounts for the latent heat released during the phase transformation from austenite to martensite.

Phase Transformation Strain

The Phase Transformation Strain is a bidirectional multiphysics coupling used to transfer strain and stress data to and from the coupled Solid Mechanics interface. When transformation-induced plasticity, thermal strains and phase plasticity are enabled in the Austenite Decomposition interface, both TRIP and thermal strains are computed and incorporated as inelastic strain contributions. Moreover, the equivalent plastic strain is transferred to the phase transformation interface, enabling the evaluation of the hardening function for each phase individually.

3.2.3 Process parameters

The main parameters used in the cooling analysis are summarized in Table 3.4. As observed, the heat transfer coefficient for natural air convection, the shaft surface emissivity and the ambient temperature remain consistent with the values adopted in the heating simulation. The quenching time is specified by the supplier, whereas the duration of the final cooling stage has been adjusted to ensure that the journal returns to ambient temperature by the end of the process. Finally, the heat transfer coefficients for spray quenching have been calibrated to replicate a surface temperature distribution during quenching that aligns with the experimental data. The resulting temperature evolution will be presented and discussed in the Results section.

Parameter	Value	Comment
h_{spray}	Curves of Figure 4.7	Heat transfer coefficients for spray quenching
h_{air}	5 W/m^{2}K	Heat transfer coefficient for air natural convection
ε_{shaft}	0.9	Emissivity of the shaft surface
t_a	20 °C	Ambient temperature
t_q	20 s	Duration of the quenching process
t_c	10 h	Duration of the final cooling process

Table 3.4: Process parameters for the cooling simulation.

3.2.4 Material properties

Unlike the induction heating analysis, the cooling study focuses on representing the microstructures separately. As a result, the material properties required by the different physics interfaces must be specified for each phase individually.
The temperature dependent trends of these properties, obtained from JMATPRO, are presented in the following figures.

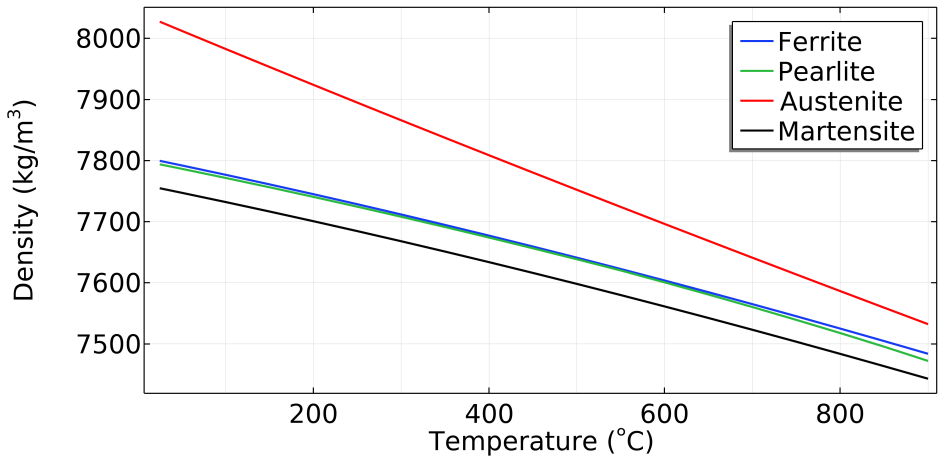

Figure 3.20: Density of 48MnVS6 microstructures as function of temperature.

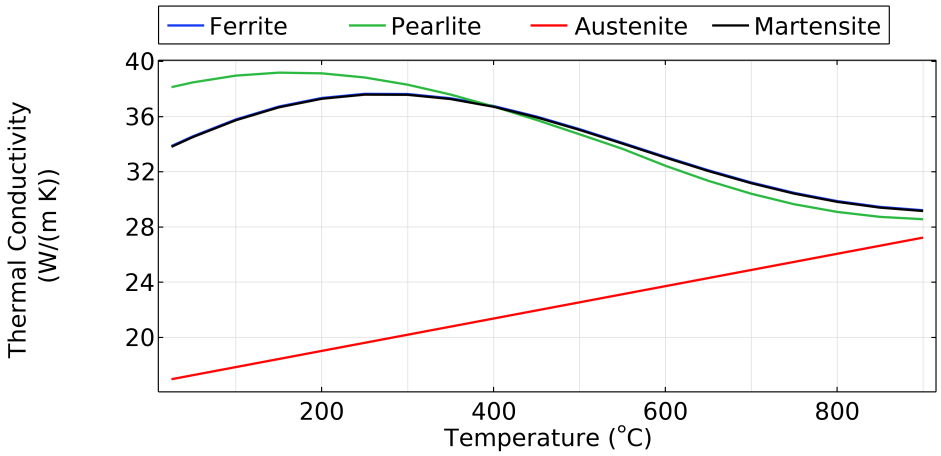

Figure 3.21: Thermal conductivity of 48MnVS6 microstructures as function of temperature.

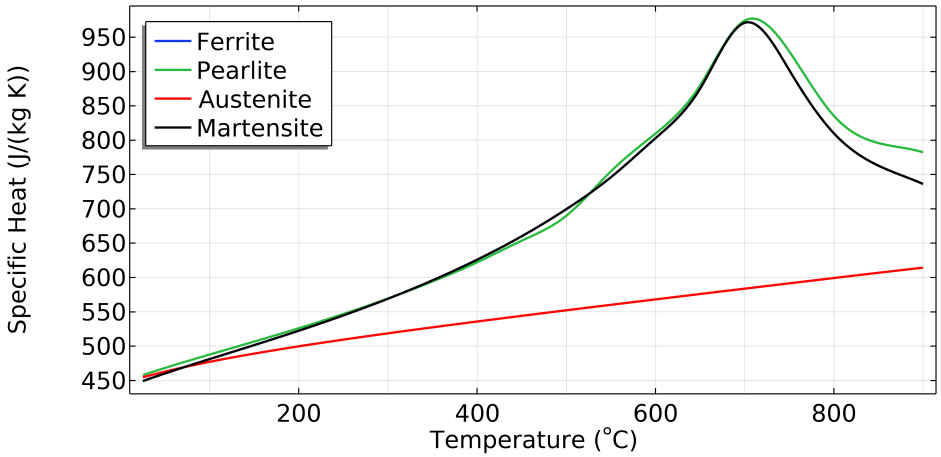

Figure 3.22: Specific heat capacity of 48MnVS6 microstructures as function of temperature.

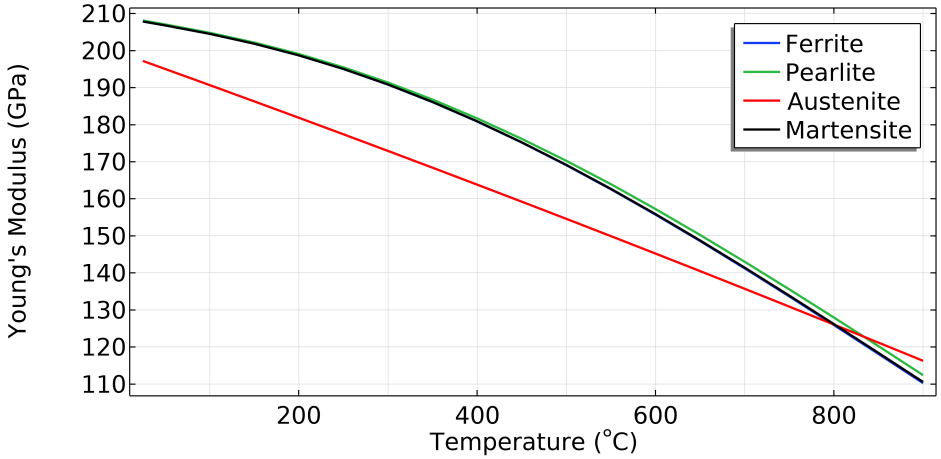

Figure 3.23: Young's modulus of 48MnVS6 microstructures as function of temperature.

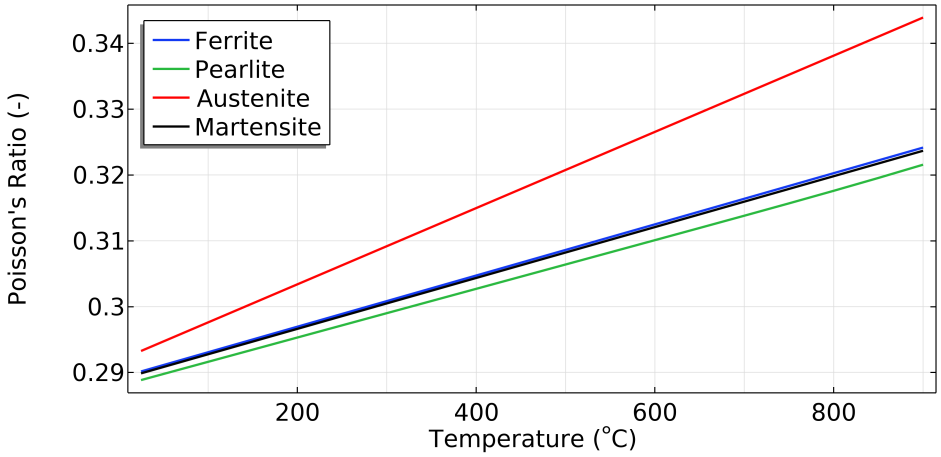

Figure 3.24: Poisson's ratio of 48MnVS6 microstructures as function of temperature.

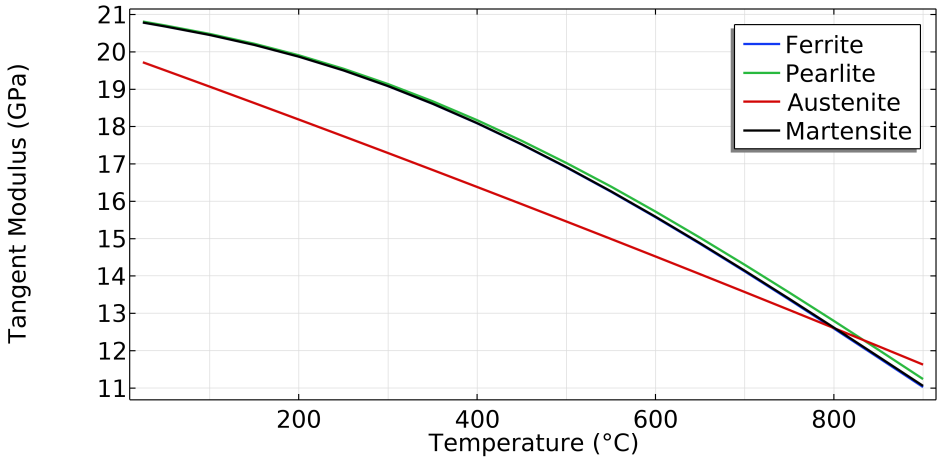

Figure 3.25: Tangent modulus of 48MnVS6 microstructures as function of temperature.

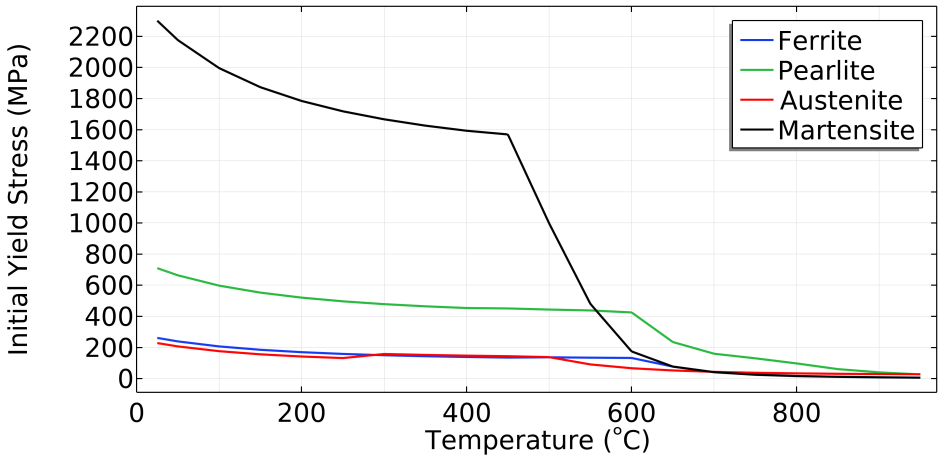

Figure 3.26: Initial yield stress of the microstructures as function of temperature.

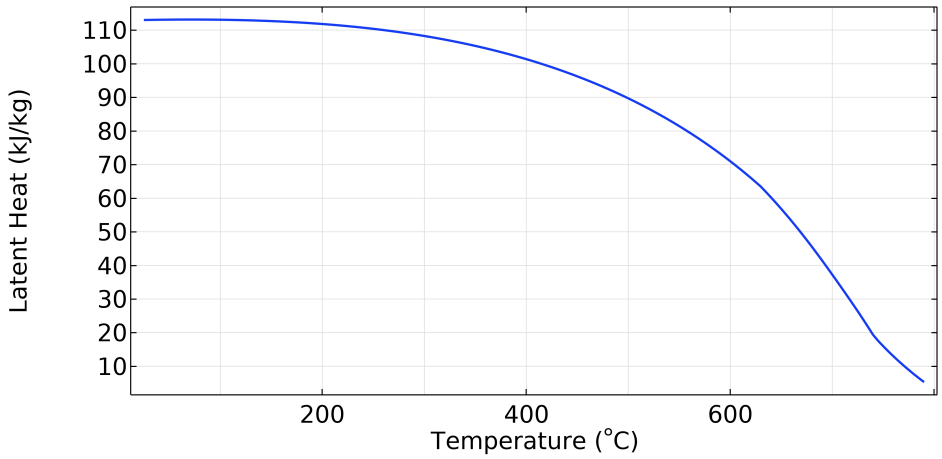

Figure 3.27: Latent heat of the austenite to martensite phase transformation in 48MnVS6 as a function of temperature.

The plot of the thermal expansion coefficient is not presented, as it has been assumed to be temperature-independent. Instead, the values for the different microstructures are provided in Table 3.5.

Microstructure	**Thermal expansion coefficient**
Austenite	$2.42 \cdot 10^{-5}$ 1/K
Ferrite-Pearlite	$1.26 \cdot 10^{-5}$ 1/K
Martensite	$1.19 \cdot 10^{-5}$ 1/K

Table 3.5: Thermal expansion coefficients for the different microstructures.

Additional material properties, primarily required by the Austenite Decomposition interface, are listed in Table 3.6.

Parameter	**Value**	**Comment**
T^{a}_{ref}	507 °C	Austenite strain-free reference temperature
$T^{f,p}_{ref}$	20 °C	Ferrite-Pearlite strain-free reference temperature
T^{m}_{ref}	50 °C	Martensite strain-free reference temperature
β	0.012 1/s	Koistinen-Marburger coefficient
M_s	334 °C	Martensite start temperature
K^{TRIP}	5· 10^{-5} 1/MPa	TRIP coefficient

Table 3.6: Material properties required by the Austenite Decomposition interface.

The material properties of each phase, along with the evolving phase composition, have been automatically used by the physics interface to compute the effective material properties. These computed properties have then been aggregated and averaged into a Compound Material, as illustrated in Figure 3.28.

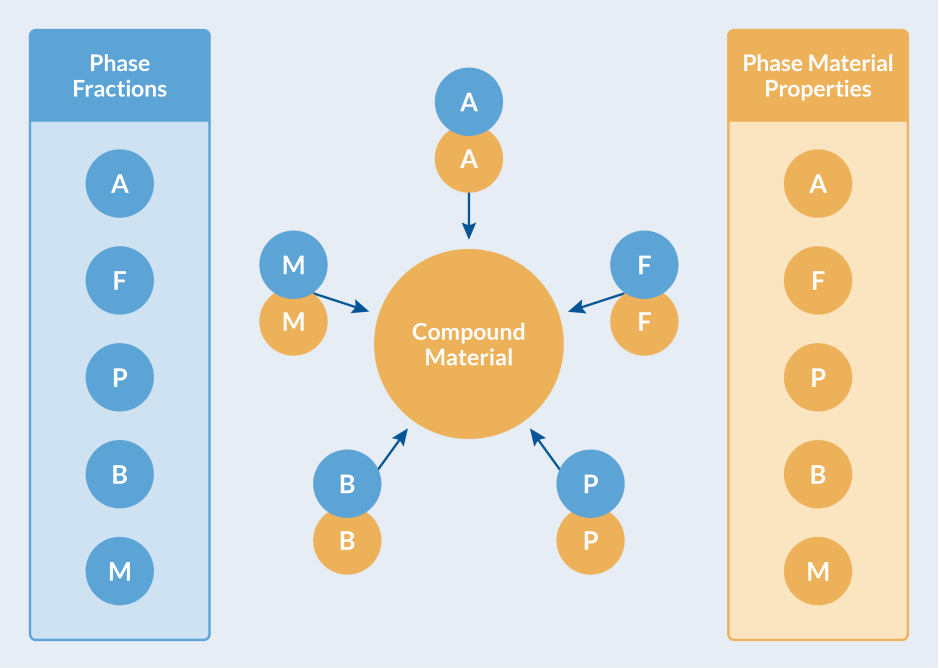

Figure 3.28: Collection of the phase properties in a compound material [8].

3.2.5 Mesh

The cooling analysis is characterized by high surface temperature gradients, but also by phase transformations. To accurately capture all these phenomena, a predefined "finer" triangular mesh with a maximum element size of 2.36 mm has been adopted. Additionally, 12 boundary layers, each with a thickness of 0.5 mm, have been implemented in the region to be hardened, ensuring an extremely fine mesh within the first 6 mm of the model. This refinement enables an accurate comparison between the hardness values obtained from the simulation and those from experimental data, which are indeed available for the first 6 mm. The resultant mesh is shown in Figure 3.29.

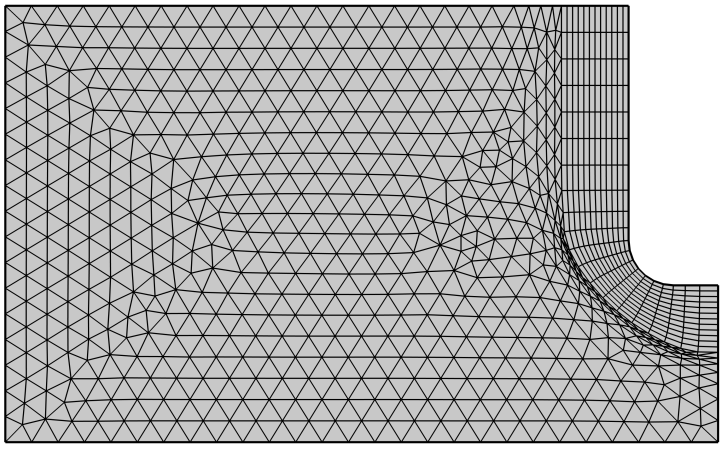

Figure 3.29: Mesh adopted for the cooling simulation.

3.2.6 Simulation procedure

The cooling analysis has been performed using two distinct Transient study steps: the first one simulates the quenching stage, while the second one models the subsequent cooling to room temperature. In both cases, a Fully Coupled approach has been employed in combination with a Direct solver, as previously discussed in Section 3.1.6. This configuration ensures robust convergence in a numerically intensive simulation involving three strongly coupled physics interfaces.

3.3 Heating time sensitivity analysis

A key factor influencing the hardening depth in induction hardening is the heating time. Extending the heating time allows the component to reach a higher temperature, thereby increasing the amount of austenite available for transformation into martensite, which results in a deeper hardening depth. This is also because a longer heating period promotes a more uniform temperature distribution within the material, facilitating a more significant phase transformation in the affected region.
To investigate this relationship quantitatively, the simulation procedure outlined in this chapter can be repeated for different heating times. After conducting these simulations, the results can be compared to assess the impact on the final hardening depth and residual stress. These comparisons will help clarify how precise control of heating time can optimize the hardening process.

Chapter 4

Results

This chapter presents and discusses the main results of the induction hardening simulation carried out on the main journal of the crankshaft. For completeness, the parameters used for the crankpin analysis, along with the main simulation results, are provided in the Appendix.

4.1 Induction heating

At the conclusion of the induction heating process, it is possible to analyze the resulting surface temperature distribution, as illustrated in Figure 4.1.

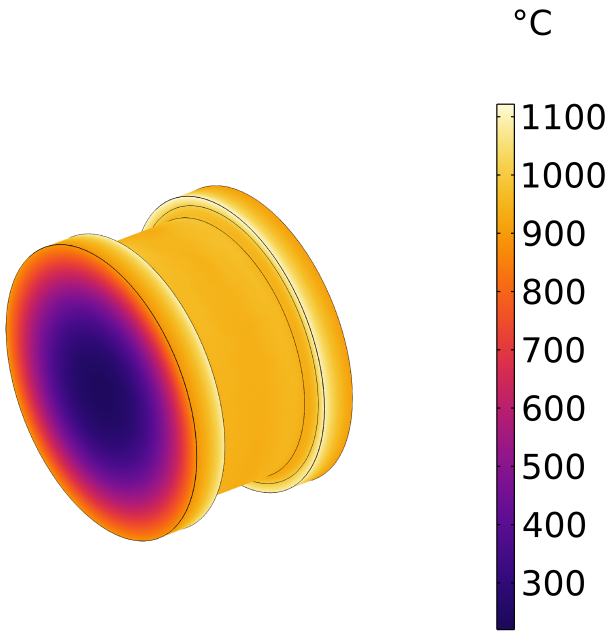

Figure 4.1: Temperature profile of the main bearing surface after heating.

It can be observed that the temperature distribution qualitatively resembles the typical profile of an induction-heated cylinder, as depicted in Figure 2.3. In fact, as expected, the surface reaches a temperature largely higher than the one at the core, which remains comparatively cooler due to the limited penetration depth of the induced currents.
However, the presence of localized hot spots suggests that analyzing the average temperature in the region targeted for hardening may provide a more representative assessment of the thermal behavior. Its evolution during the heating process is presented in Figure 4.2.

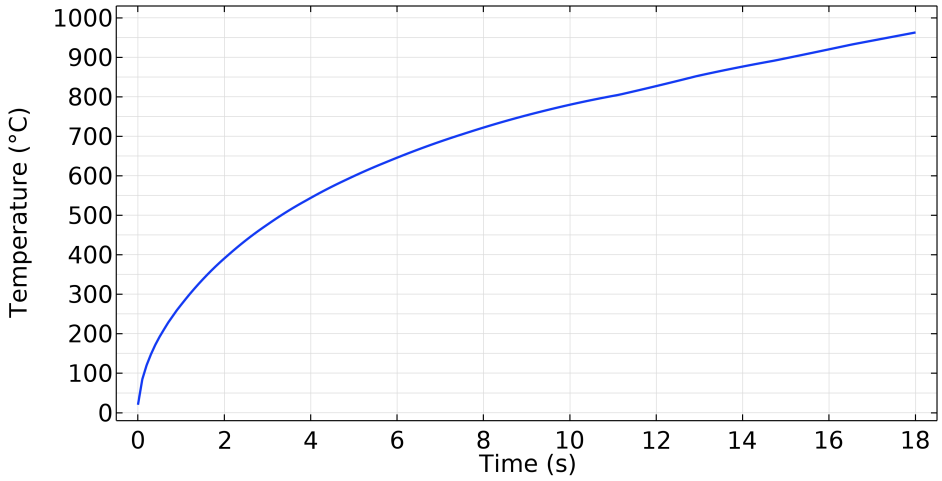

Figure 4.2: Average temperature variation of the main bearing surface during heating.

As shown, after 18 seconds the average surface temperature approaches 1000 °C, exceeding the austenitization threshold of approximately 730 °C, as indicated in Figure 3.10.
To gain further insight into the internal temperature distribution, Figure 4.3, which illustrates a cross-sectional view of half the crankshaft, can be analyzed.

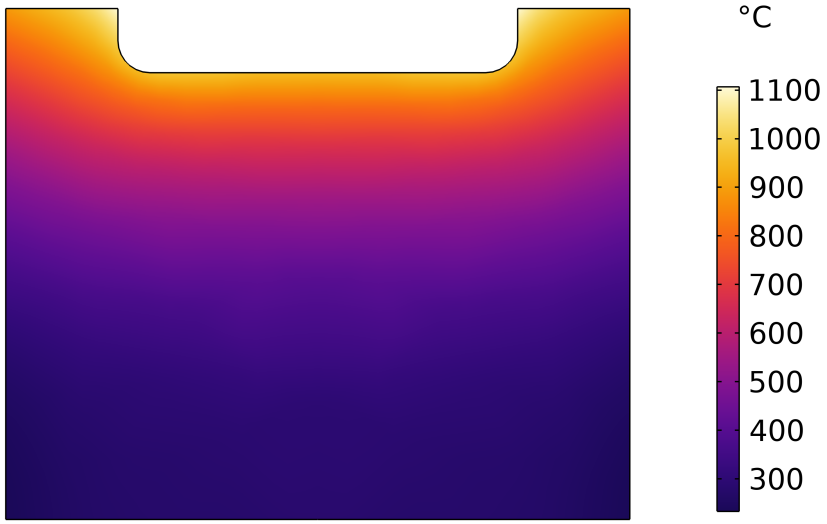

Figure 4.3: Temperature profile across the main bearing after heating.

This visualization allows for a more comprehensive evaluation of the thermal gradient from the surface to the core, making evident that only the region near the surface exceeds the phase transformation temperature. The rest of the component remains below this critical value, thereby retaining its initial ferritic-pearlitic microstructure. This observation can be further validated by plotting the temperature-dependent phase fraction of austenite, obtained using JMATPRO, across the cross-section of the shaft. The resulting distribution, shown in Figure 4.4, confirms the presence of a high austenite fraction near the surface, which rapidly diminishes when moving toward the core. This trend is consistent with the thermal gradient observed in the temperature profile and further highlights the localized nature of the induction heating process.

Figure 4.4: Austenite distribution across the main bearing after heating.

4.2 Cooling

The cooling process requires the definition of heat transfer coefficients that accurately represent the effect of spray quenching. As discussed in Section 3.2.3, these parameters have been calibrated to reproduce a surface temperature profile in the hardened region that closely matches experimental measurements. The comparison between the simulated cooling curves and the experimental results is shown in Figures 4.5 and 4.6, while the final heat transfer coefficients, used at three different locations, are presented in Figure 4.7.

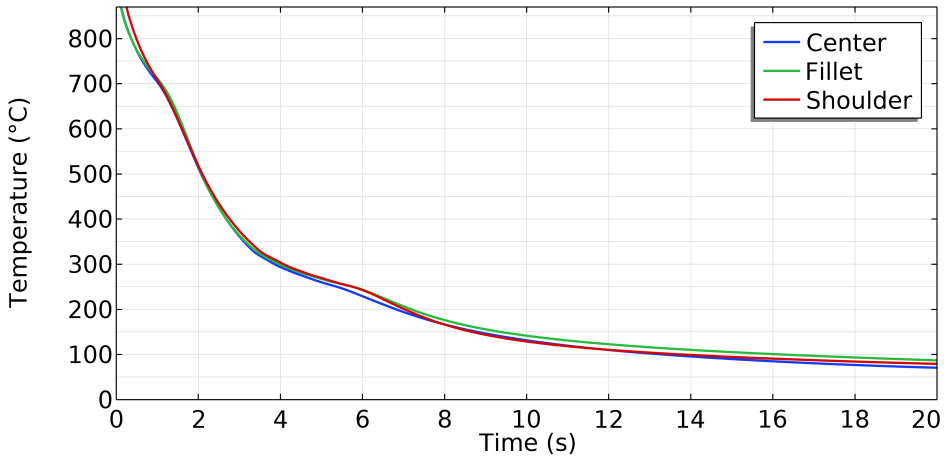

Figure 4.5: Average temperature variation of the main bearing surface temperature during quenching (simulation).

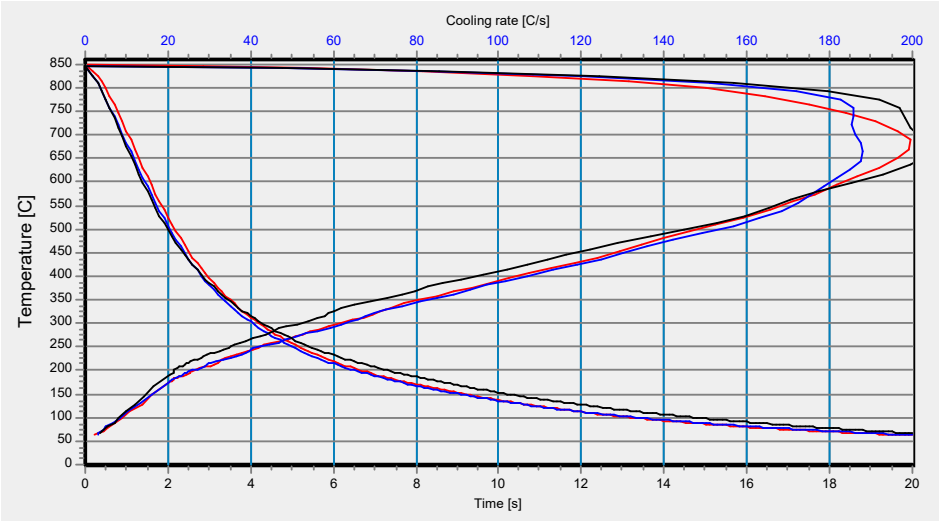

Figure 4.6: Average temperature variation of the main bearing surface temperature during quenching (experiment).

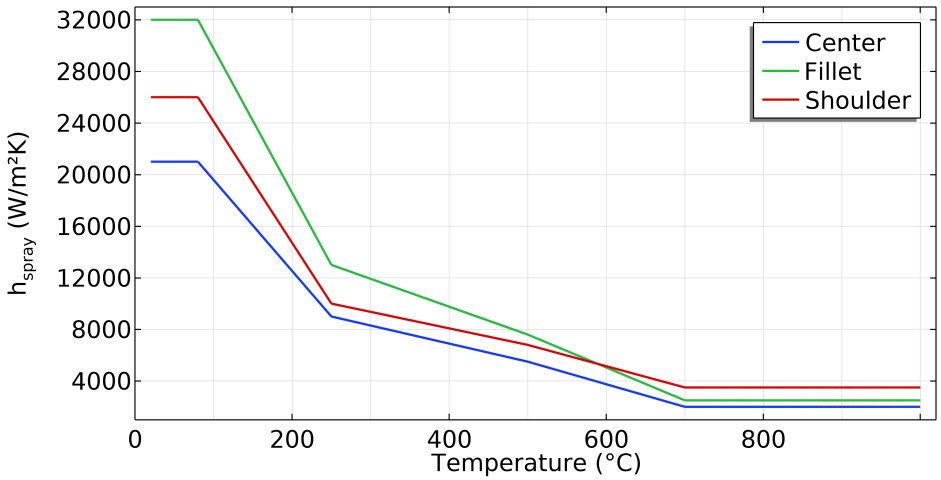

Figure 4.7: Heat transfer coefficients calibrated for the quenching simulation of the main bearing.

Using the selected heat transfer coefficient, the component can be successfully quenched. As a result, a portion of the austenite transforms into martensite, whose distribution is illustrated in Figure 4.8.

Figure 4.8: Martensite distribution across the main bearing.

It should be noted that not all the austenite shown in Figure 4.4 has been transformed into martensite. This is due to the application of the heat transfer coefficients being limited only to the region intended for hardening.
Based on the resulting microstructure, the hardness distribution within the material can be evaluated. As expected, Figure 4.9 indicates high hardness values at the surface, which decrease rapidly toward the core. This trend correlates with the distribution of martensite in the crankshaft.

Figure 4.9: Vickers hardness profile across the main bearing.

A preliminary assessment of the simulation's accuracy can be carried out by identifying the region where the hardness exceeds the threshold value specified by the requirements, set at 400 HV. As highlighted in yellow in Figure 4.10, the resulting profile qualitatively resembles the hardened layer shown in Figure 2.11.

Figure 4.10: Area with hardness exceeding the critical threshold.

However, to gain quantitative information, it is necessary to compare the experimental hardness profile with the results coming from the simulation. A comparison executed at the centerline of the journal is shown in Figure 4.11.

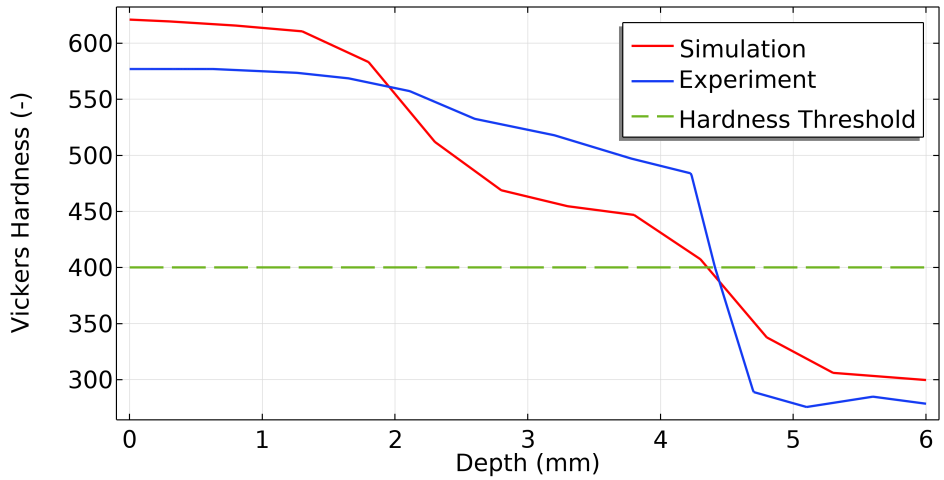

Figure 4.11: Comparison of the hardness profiles along the centerline of the main bearing.

To correctly interpret the previous figure, it is important to note that the measured hardness values refer to a crankshaft that has undergone tempering and grinding processes. The tempering treatment serves to relieve internal stresses and reduces the material hardness by approximately 20 HV, which may explain the higher values predicted by the simulation at the surface and beyond the hardness threshold.
Subsequently, the grinding process removes approximately 0.7 mm from the surface. Consequently, in order to account for the material removal during grinding, the simulated hardness values have been evaluated starting from a depth of 0.7 mm. Furthermore, the alloy composition used in the model is based on average weight percentages specified in the material standard, rather than the precise chemical composition of the tested component.
Despite these discrepancies, the simulation shows good agreement with the experimental data. The specified hardness threshold, also called hardening depth, has been achieved at 4.35 mm in the simulation and 4.40 mm in the experimental results. However, a region of lower-than-expected hardness is observed at a depth between 2 mm and 4.40 mm. This deviation may be attributed to limitations of the Impedance Boundary Condition applied in the simulation, which does not fully resolve the skin depth. As a result, the predicted temperature in this region is lower, leading to a reduced austenite fraction available for transformation into martensite.
A similar comparison can be performed at the fillet region, following the red line shown in Figure 4.12.

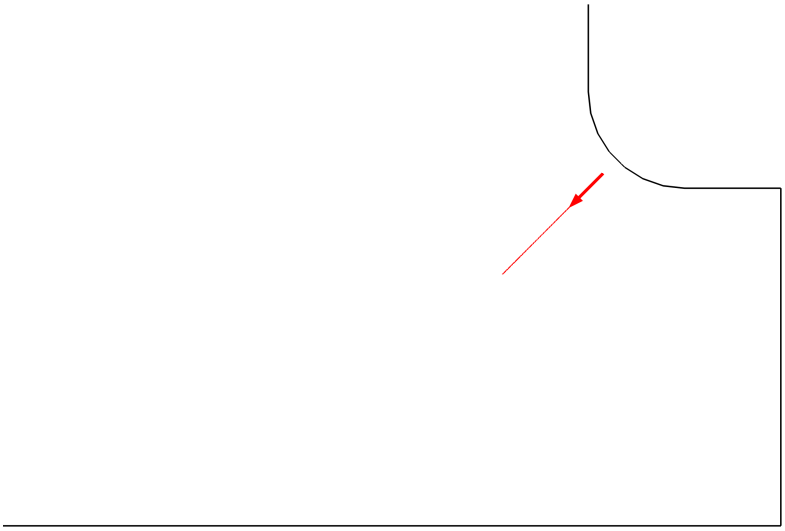

Figure 4.12: Direction for evaluation of the fillet hardness.

The results obtained at this location are presented in Figure 4.13.

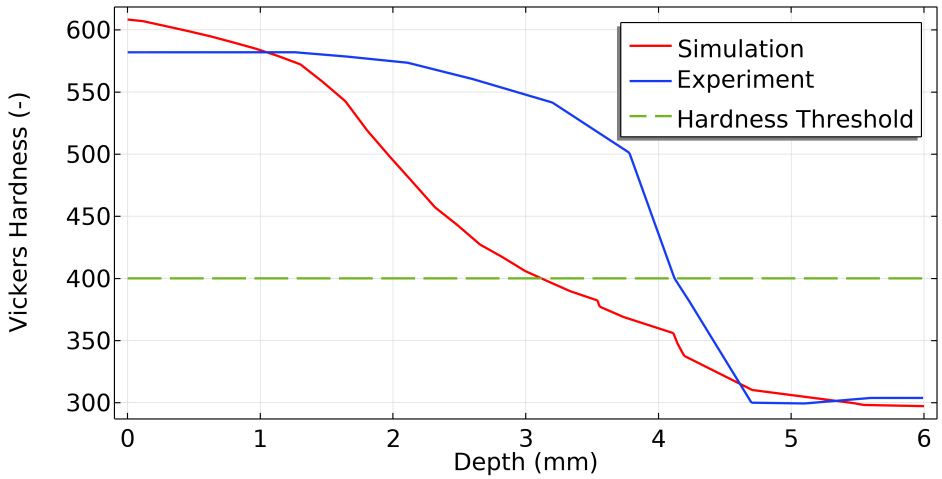

Figure 4.13: Comparison of the hardness profiles at the fillet of the main bearing.

It can be observed that the hardness achieved at the fillet is lower than expected, particularly regarding the predicted depth at which the limiting value is reached, being 3.10 mm compared to the expected 4.10 mm. This discrepancy may arise from the fact that, as shown in Figure 4.14, not all the available austenite has been transformed into martensite, which is the primary microstructure responsible for the increase in hardness.

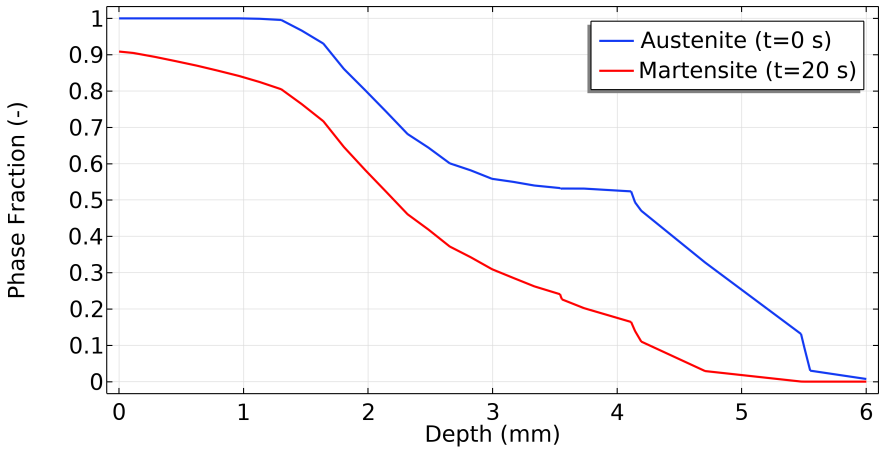

Figure 4.14: Initial austenite and final martensite phase fractions at the fillet of the main bearing.

Conversely, Figure 4.15 shows that nearly all the available austenite at the centerline has been transformed into martensite, which explains the better results achieved at this location.

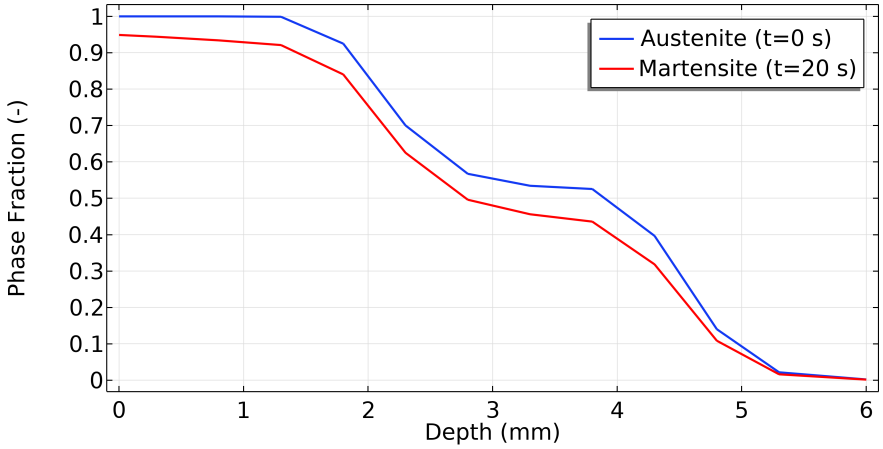

Figure 4.15: Initial austenite and final martensite phase fractions along the centerline of the main bearing.

This discrepancy can be attributed to the calibration method adopted for the heat transfer coefficients, which has been based on an average surface temperature profile recorded during the quenching phase. While this approach yields accurate results at the centerline, it underestimates the heat transfer coefficient at the fillet, leading to a reduced formation of martensite in this region. However, since no additional data are available to calibrate the heat transfer coefficient at this location, only a qualitative analysis of the effect of increasing this parameter can be performed, for instance by doubling its value. This adjustment results in a higher martensite fraction and, consequently, an increase in hardness, as shown in Figure 4.16. As a consequence, the depth at which the hardness threshold has been reached increases from 3.10 mm to 4.20 mm.

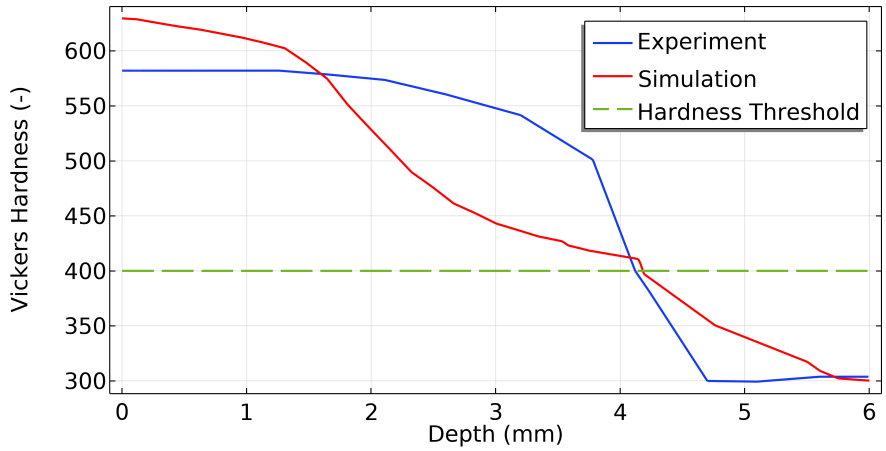

Figure 4.16: Comparison of the hardness profiles at the fillet of the main bearing with a higher heat transfer coefficient.

In conclusion, it is possible to evaluate the residual stress profile along the centerline of the crankshaft. Figure 4.17 illustrates the three main tension components: radial, axial and circumferential. As expected, the radial stress is zero at the surface, since the main bearing is free to expand in this direction. In contrast, both axial and circumferential tensions are compressive at the surface, resulting from the martensitic transformation. This compressive stress is counterbalanced by a tensile stress within the material, located just beyond the hardened layer, with a peak axial value of 470 MPa at a depth of 5.30 mm.
Notably, the maximum compressive stress in the circumferential direction at the surface is particularly high, reaching approximately -1200 MPa. This value exceeds experimental measurements, which show a maximum of about -1000 MPa after tempering and grinding. The discrepancy may arise from the relaxation caused by tempering and the assumption used in the simulation regarding the plastic deformation of the material. In fact, the isotropic tangent modulus has been set at 10% of the Young's modulus, a common practice that may not accurately capture the material's hardening behavior.

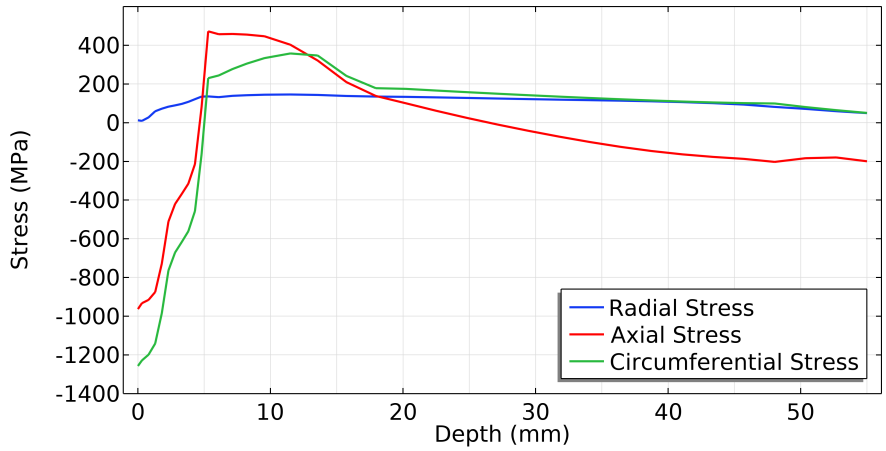

Figure 4.17: Residual stress components along the centerline of the main bearing.

4.3 Heating time sensitivity analysis

The results in terms of hardness profile along the crankshaft centerline for heating times ranging from 16 s to 20 s are presented in Figure 4.18.

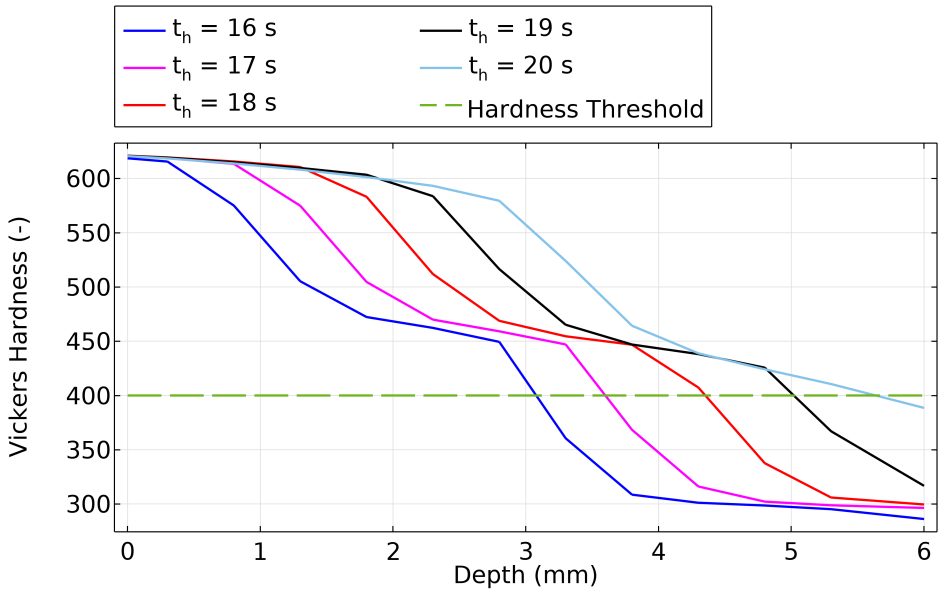

Figure 4.18: Comparison of the hardness profiles along the centerline of the main bearing for different heating times.

As expected, the previous figure shows that increasing the heating time results in a higher overall hardness, shifting the depth at which the threshold is reached to greater values. Conversely, a shorter heating process yields the opposite effect.
For further insight, Figure 4.19 illustrates an almost linear relationship between heating time and hardening depth.

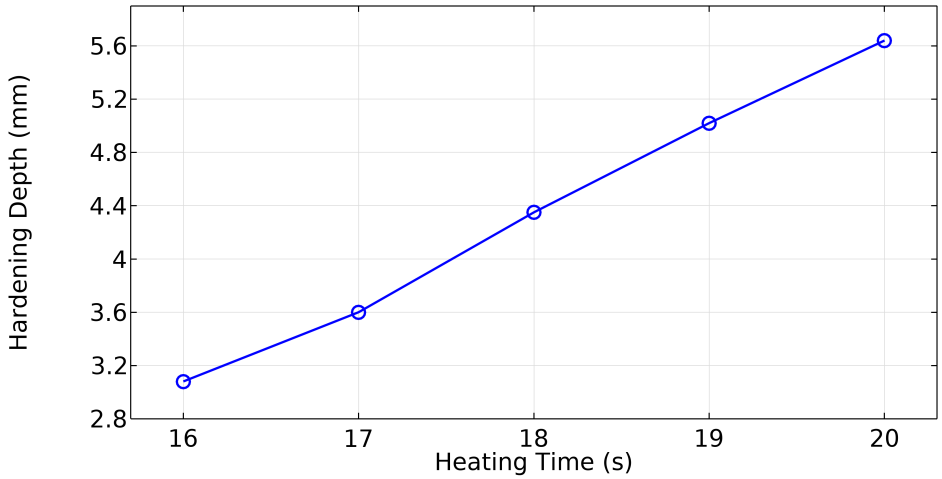

Figure 4.19: Hardening depth along the centerline of the main bearing for different heating times.

Additionally, evaluating the effect of heating time on the residual stress distribution provides valuable insights into the mechanical response of the component. For this purpose, a comparison of the mean residual stress, described in Eq.(4.1), is carried out, as illustrated in Figure 4.20.

$$S_m = \frac{1}{3}\left(S_{rr} + S_{zz} + S_{\theta\theta}\right), \tag{4.1}$$

where S_{rr}, S_{zz} and $S_{\theta\theta}$ are the radial, axial and circumferential components of the stress tensor, respectively.
This analysis offers a global perspective on how the stress state evolves as the heating time is varied since, as shown in the previous equation, the mean stress averages the overall stress distribution across the section.

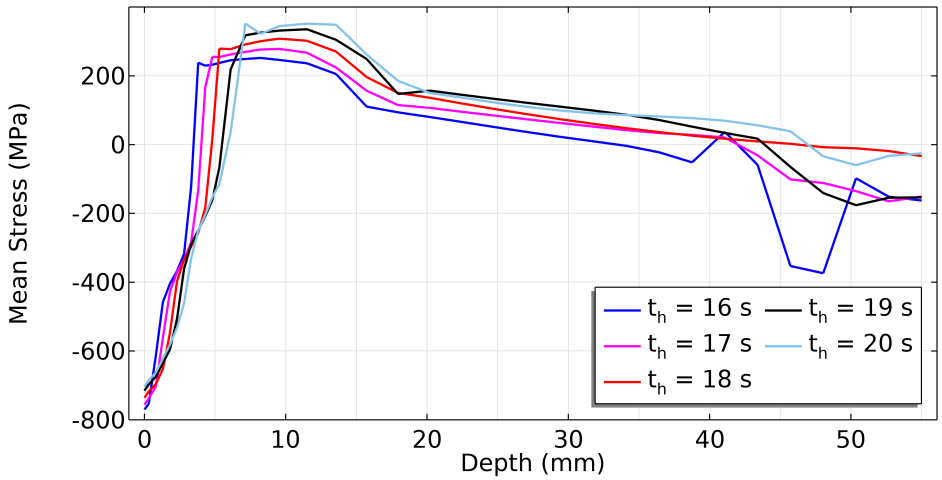

Figure 4.20: Comparison of the mean stress along the centerline of the main bearing for different heating times.

From the previous figure one can state that as the induction heating time increases, the maximum compressive stress at the surface slightly decreases. This behavior can be attributed to the deeper penetration of thermal energy, which leads to a thicker austenitized and subsequently martensitic layer. As a result, the compressive stresses associated with the volumetric expansion during phase transformation are distributed over a greater depth, reducing their intensity at the surface. Furthermore, the extended thermal exposure may cause partial stress relaxation, contributing to the observed reduction. In parallel, the tensile stress peak shifts to a greater depth and reaches a higher magnitude, in order to maintain equilibrium with the enlarged hardened zone.

Chapter 5

Final Remarks

5.1 Conclusion

In this thesis, a numerical model of the induction hardening process was developed for the crankshaft of the 6 cylinder, 13 liter Scania Super engine, produced by the Swedish heavy-duty truck manufacturer Scania. The simulation was performed using the finite element solver COMSOL Multiphysics version 6.3, aiming to simulate the heat treatment from electromagnetic, thermal, microstructural and mechanical perspectives.
The simulation involved the coupled modeling of various physical phenomena using the multiphysics interfaces provided by COMSOL. The Magnetic Fields module was used to solve the Maxwell's equations in the frequency domain, accounting for the electromagnetic field generated by the coil and the induced eddy currents in the crankshaft. Heat transfer modeling incorporated the heat generated through induction, as well as cooling effects due to air convection, radiation and spray quenching. Phase transformations were considered only during the quenching stage, using the Koistinen–Marburger model to describe the austenite to martensite transition, implemented through the Austenite Decomposition interface. Finally, the Solid Mechanics features enabled the solution of the equation of motion and the computation of residual stresses in the three main directions.
The analysis was conducted using the real coil geometry, which is critical for accurate results. In fact, preliminary simulations employing a simplified inductor geometry required current magnitudes substantially higher than the interval specified by the supplier, ranging from 3 to 8 kA. In contrast, using the actual coil geometry resulted in a current value of 7.1 kA, that conforms to the specified range, demonstrating the importance of geometric fidelity in the simulation. Conversely, a simplified configuration was adopted for the journal to exploit axial symmetry and reduce computational complexity.
Several process parameters were required to simulate the induction hardening process. These quantities were either provided by the supplier, derived from industrial practice, or adjusted to obtain reasonable results, as discussed in Sections 3.1 and 3.4. Material properties were defined using JMATPRO version 12.4. Particular attention was given to mesh design in order to achieve an optimal balance between computational accuracy and efficiency.

The results obtained, in terms of temperature distribution, hardness profile, residual stresses within the hardened layer and effect of heating duration, qualitatively showed good agreement with the expected physical behavior described in Section 2.2. The inductive heating effect proved to be highly localized, with heat concentrated near the surface of the workpiece due to the skin effect. This led to a non uniform temperature distribution and resulted in a high hardness region near the surface, where significant compressive residual stresses were also observed. The core instead remained unhardened, retaining the initial microstructure. Moreover, the results were validated against available experimental measurements, including the surface cooling curve, the hardness profile within the first 6 mm of the journal along the centerline and at the fillet, as well as the maximum compressive stress achieved at the surface. This comparison demonstrated that the adopted methodology yields good agreement between the simulation results and the experimental data. The cooling curve closely matched the actual temperature measurements during quenching, while only minor discrepancies were observed in the hardness profiles. Finally, the predicted maximum surface compressive stress was in reasonable agreement with the measured value. Moreover, both the hardness profile and the residual stress distribution are consistent with findings reported in similar studies (Ref. [12] - [23]). In these cases, a high surface hardness is observed, which decreases sharply within the first few millimeters. Additionally, the residual stress profile exhibits a maximum compressive stress of approximately –1000 MPa at the surface, transitioning to tensile stresses just beyond the hardened layer. In this tensile region, the stress reaches a peak ranging between 350 MPa and 600 MPa. This values correlates well with the results obtained in the present work.

5.2 Discussion

The methodology discussed in the report can also be extended to other surfaces of the crankshaft, such as the crankpin, whose results are presented in Appendix A, by adapting the geometry and adjusting the process parameters. Specifically, it is first necessary to select the current frequency, induction heating time and quenching duration based on the data provided by the supplier for the specific journal to be hardened. The coil current must then be tuned based on the resulting surface temperature and the thickness of the austenitic layer, which in turn determines the martensite penetration and thus the hardness profile, the primary quantity used for comparison with experimental data. Additionally, the heat transfer coefficients for quenching need to be updated and calibrated to match the experimental cooling curve. The remaining parameters can be retained as defined in this report, since they apply to the entire crankshaft rather than to an individual journal. However, if the simulation is extended to a different shaft, these parameters must be adjusted accordingly based on the specific conditions applicable to that particular component.
Despite its versatility and promising results, the methodology is subject to a number of limitations that affect the accuracy and applicability of the simulation, primarily arising from the following simplifications:

- Use of a simplified geometry for the crankshaft journal, which affects the dis-

tribution of thermal and electromagnetic fields, reducing accuracy during both heating and cooling.

- Adoption of global material properties during induction heating, without differentiating between the various microstructural phases. This neglects the distinct behavior of different metallurgical structures.
- Neglect of the austenite to ferrite-pearlite transformation during both heating and cooling.
- Application of the impedance boundary condition to model induction heating instead of solving Maxwell's equations directly within the crankshaft. This confines the heating effect to the surface and underestimates the heat penetration into the material.
- Employment of the Solid with Translational Motion interface instead of a moving mesh.
- Use of average weight percentages of the alloying elements instead of the real values.
- Use of a default value for the TRIP coefficient.
- Adoption of a standard value for the tangent modulus due to the lack of information on the plastic behavior of the different steel phases.

Considering the limitations discussed above, future improvements may concentrate on the following areas:

- Implementation of a more realistic crankshaft geometry to improve the accuracy of the thermal and electromagnetic field distribution.
- Modeling of the full microstructural evolution during both heating and cooling phases.
- Solution of Maxwell's equations directly within the crankshaft using the Ampère's Law in Solids condition, in order to resolve the complete skin depth.
- Use of the Rotating Machinery Magnetic interface, combined with a moving mesh, to simulate the actual rotation of the component and to account for its deformation. This approach enables the distribution of eddy currents, and consequently heat generation, around the entire circumference of the journal, eliminating the need for an artificial advective heat transfer term. As a result, this method has the potential to improve the accuracy of the thermal field during the induction heating stage. However, it requires an extremely fine mesh at the interface between the rotating and stationary domains, which significantly increases the computational time.
- Acquisition of more detailed information about the material, including exact alloying element percentages, plastic deformation behavior and hardening fuction.

Appendix A: Crankpin analysis

The same methodology utilized for the main journal can be applied to simulate the induction hardening of the crankpin, specifically the sixth one. However, modifications to the geometry and process parameters are required. The updated parameters are summarized in Table A.1.

Parameter	Value	Comment
I_{coil}	6.8 kA	Electric current supplied to the coil
f	9.5 kHz	Frequency of the coil current
ω	60 rad/s	Rotational speed to induce the advective heat transfer
h_{air}	5 W/m^{2}K	Heat transfer coefficient for air natural convection
ε_{shaft}	0.9	Emissivity of the shaft surface
t_a	20 °C	Ambient temperature
t_i	20 °C	Initial temperature of the shaft
t_h	16 s	Duration of the heating process
h_{spray}	Curves of Figure A.6	Heat transfer coefficients for spray quenching
t_q	20 s	Duration of the quenching process
t_c	10 h	Duration of the final cooling process

Table A.1: Process parameters for the induction hardening simulation of the crankpin.

The following sections briefly present the main simulation results for the sixth crankpin, covering the induction heating and cooling processes, as well as a sensitivity analysis on heating time.

A.1 Induction heating

As with the main bearing, the induction heating process leads to a significant temperature gradient between the crankpin surface and its core. At the end of heating, the surface temperature has exceeded the austenitization threshold, whereas the core has remained substantially cooler, as illustrated in Figure A.1.

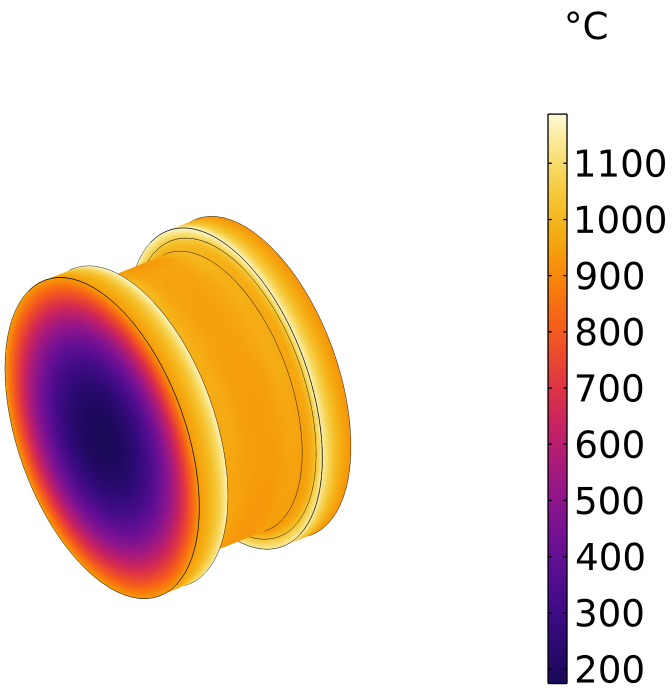

Figure A.1: Temperature profile of the crankpin surface after heating.

The global surface temperature evolution is shown in Figure A.2, which highlights the rapid heating rate and its variation over time.

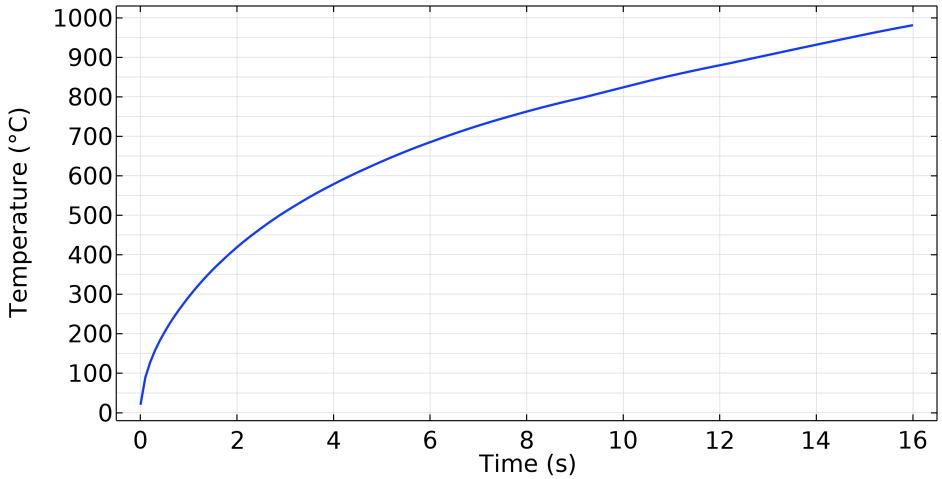

Figure A.2: Average temperature variation of the crankpin surface during heating.

As expected, only a shallow layer near the surface has reached high temperatures, with a rapid drop toward the interior. This is depicted in Figure A.3, and it reflects the localized formation of austenite, as shown in Figure A.4.

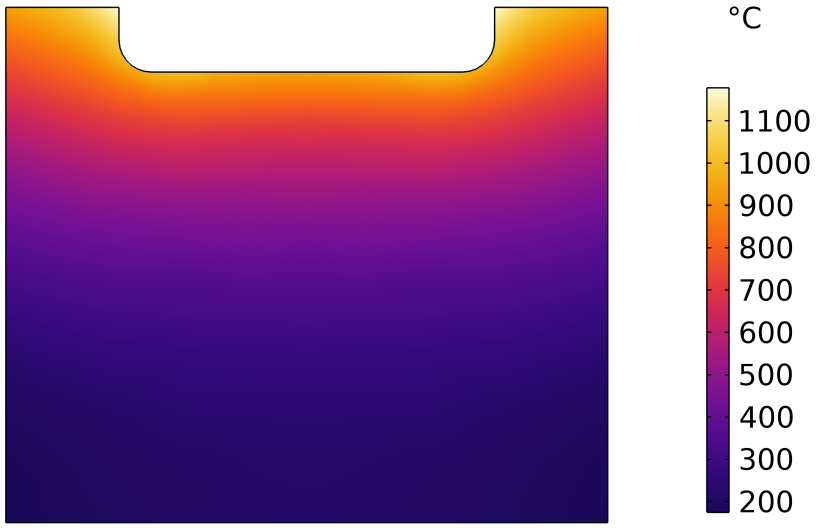

Figure A.3: Temperature profile across the crankpin after heating.

Figure A.4: Austenite distribution across the crankpin after heating.

A.2 Cooling

Following heating, the crankpin undergoes cooling. As with the main bearing, the heat transfer coefficients have been calibrated to align the cooling profile with experimental data. The resulting cooling curves and calibrated HTCs are shown in Figures A.5 and A.6, respectively.

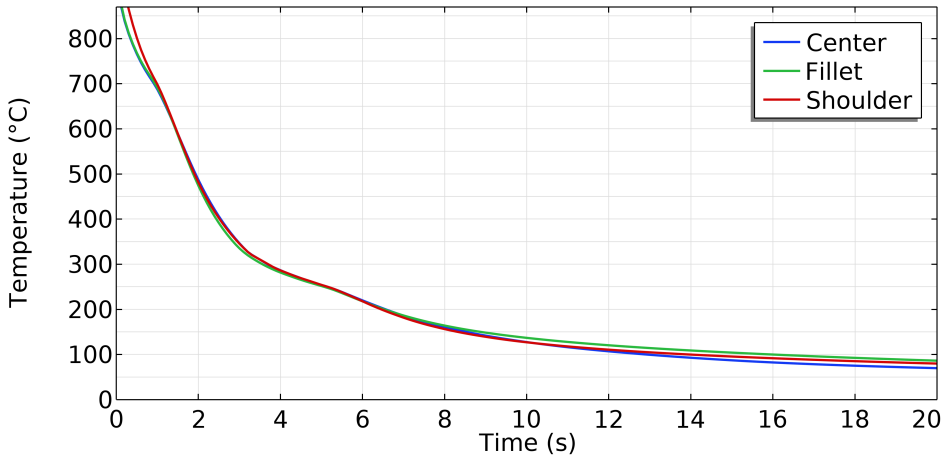

Figure A.5: Average temperature variation of the crankpin surface temperature during quenching.

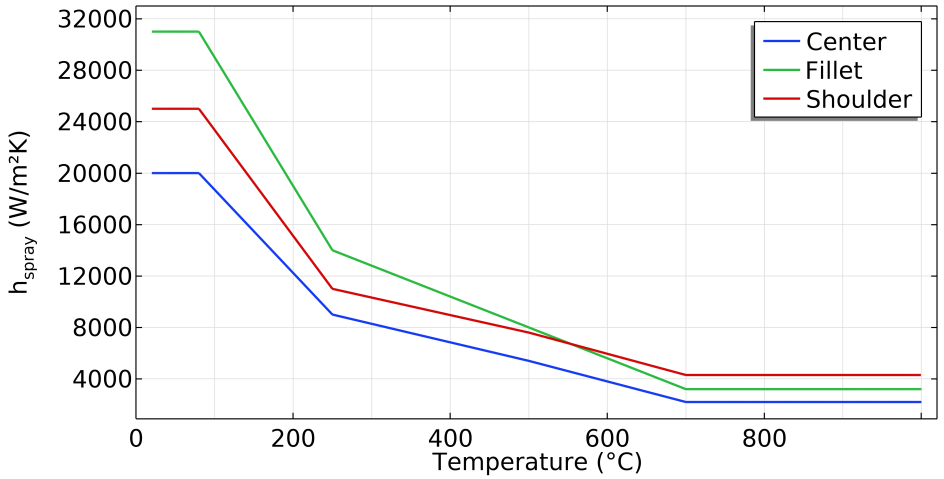

Figure A.6: Heat transfer coefficients calibrated for the quenching simulation of the crankpin.

As a result of quenching, the austenite has transformed into martensite, whose distribution is shown in Figure A.7.

Figure A.7: Martensite distribution across the crankpin after heating.

Consequently, high hardness has been achieved near the surface, while the core has remained unhardened. This behavior is demonstrated in Figure A.8.

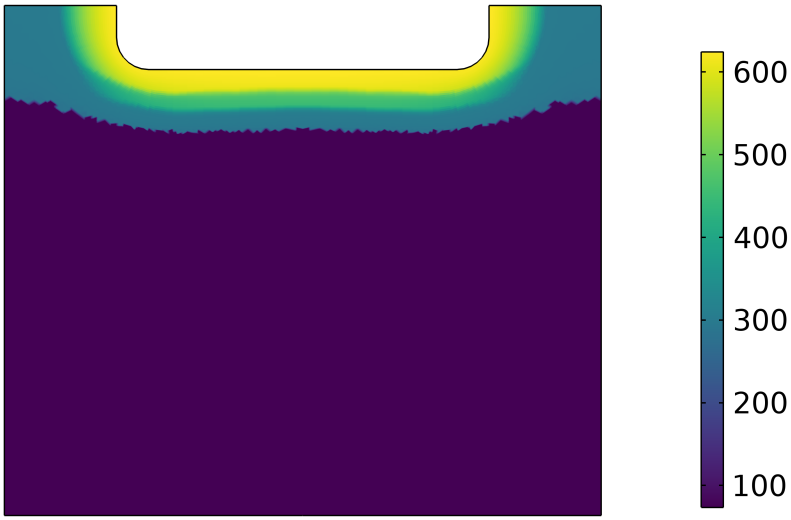

Figure A.8: Vickers Hardness profile across the crankpin.

Simulation results are compared with experimental hardness profiles at both the centerline and fillet regions of the crankpin, as shown in Figures A.9 and A.10.

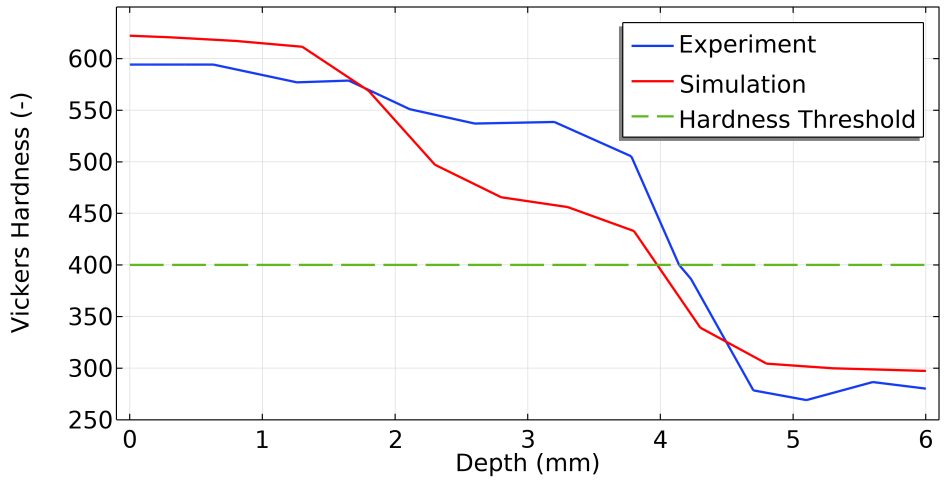

Figure A.9: Comparison of the hardness profiles along the centerline of the crankpin.

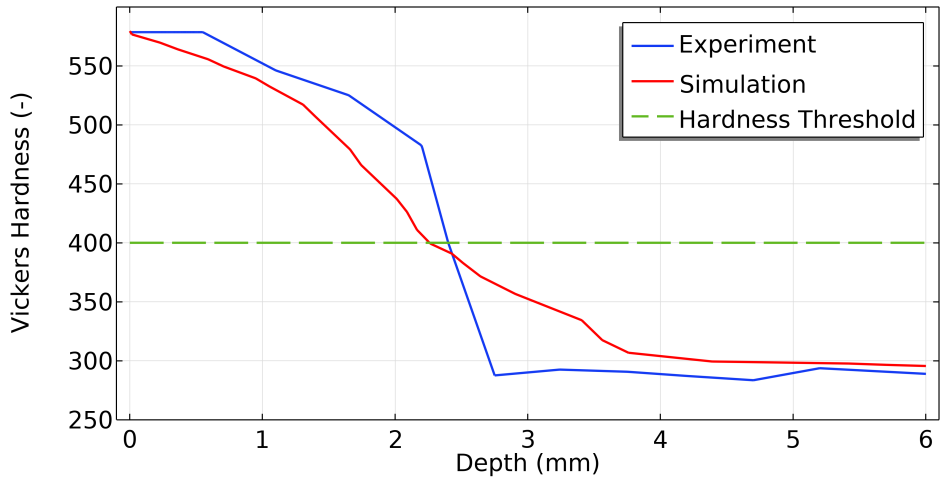

Figure A.10: Comparison of the hardness profiles at the fillet of the crankpin.

The same observations made for the main bearing apply here. Specifically, the simulation accurately predicts surface hardness and hardening depth, but discrepancies arise in the transition area. This may be attributed to the impedance boundary condition used in the electromagnetic model, which confines the heating power near the surface and limits internal temperature rise, thus reducing austenite formation in the deeper layers.
Residual stress profiles have also been evaluated, and results for the three main directions are reported in Figure A.11. As in the main bearing, radial stress at the surface is null, while compressive stresses dominate the circumferential and axial directions. Also in this case, the peak compressive stress exceeds experimental values, reaching approximately –1200 MPa. The tensile axial stress peaks at 536 MPa, located at a depth of 4.6 mm, just beyond the hardened region.

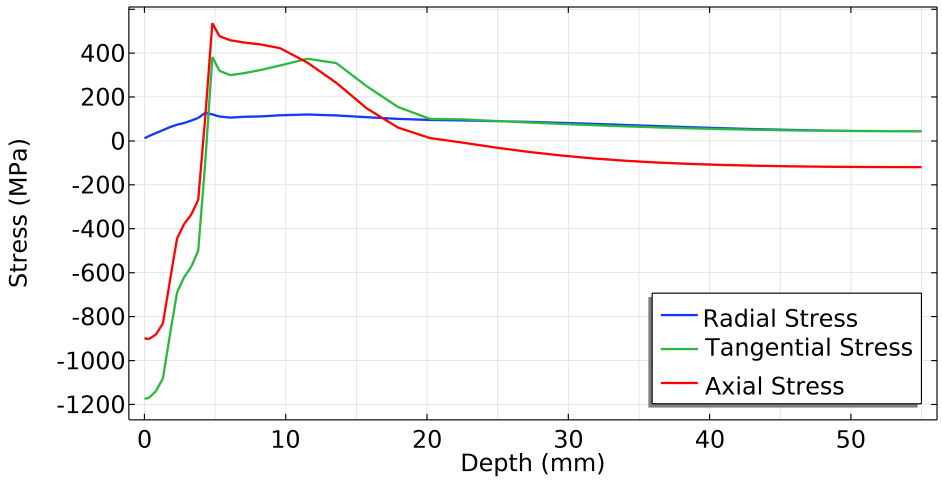

Figure A.11: Residual stress components along the centerline of the crankpin.

A.3 Heating time sensitivity analysis

The sensitivity analysis confirms that an increase in heating time results in higher surface hardness (Figure A.12) and greater hardening depth (Figure A.13), which increases almost linearly with time.

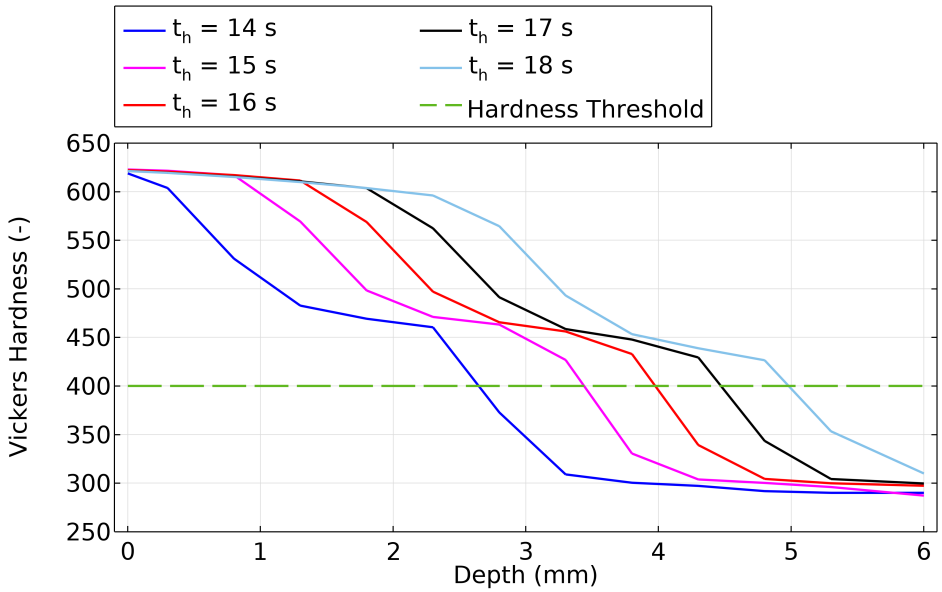

Figure A.12: Comparison of the hardness profiles along the centerline of the crankpin for different heating times.

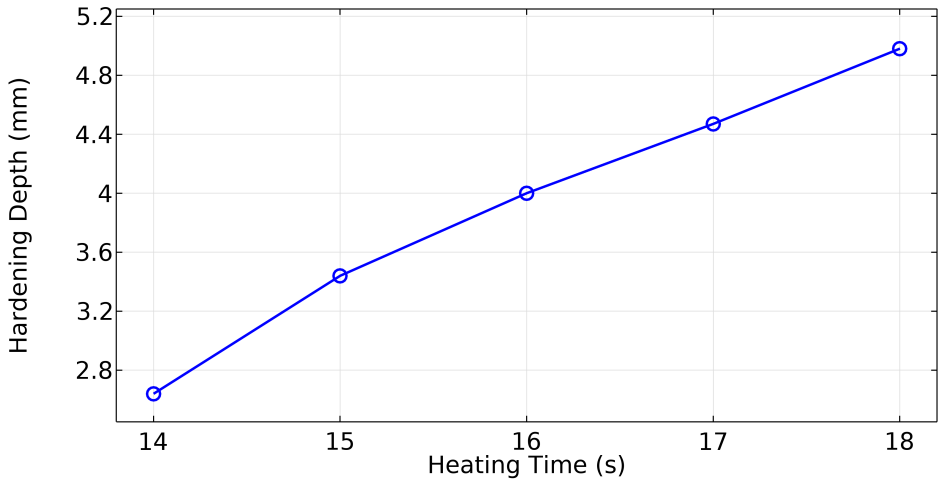

Figure A.13: Hardening depth along the centerline of the crankpin for different heating times.

The influence of heating time on residual stress is illustrated in Figure A.14. A longer duration decreases the peak compressive stress at the surface while increasing the extent of the compressive region. As a consequence, the tensile stress peak shifts to a greater depth and grows in magnitude.

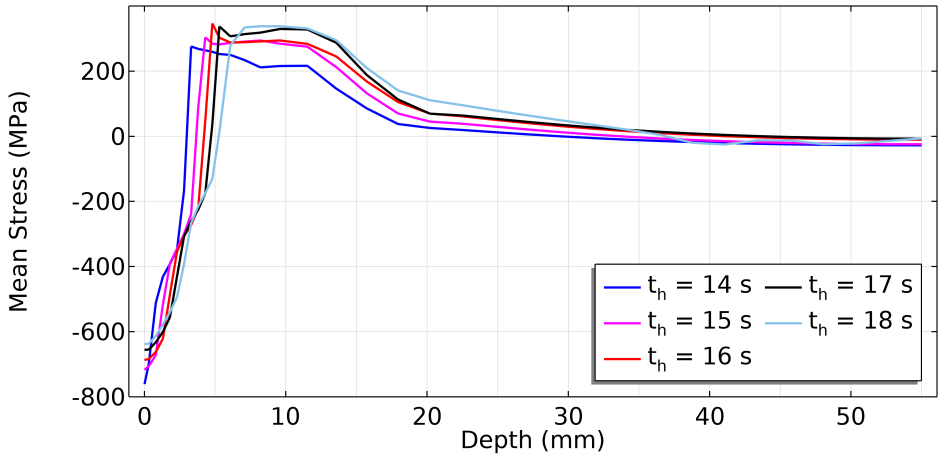

Figure A.14: Comparison of the mean stress along the centerline of the crankpin for different heating times.

References

[1] COMSOL AB. *AC/DC Module User's Guide*, 2024.

[2] COMSOL AB. *Heat Transfer Module User's Guide*, 2024.

[3] COMSOL AB. *Metal Processing Module User's Guide*, 2024.

[4] COMSOL AB. *Structural Mechanics Module User's Guide*, 2024.

[5] COMSOL AB. *Understanding the Fully Coupled vs. Segregated Approach and Direct vs. Iterative Linear Solvers*. Comsol Support, 2024.

[6] K.W. Andrews. *Empirical formulae for the calculation of some transformation temperatures*. Journal of the Iron and Steel Institute, 203:721–727, 1965.

[7] Open Courses. *Material Science - 1 | C8-L3 | Definition of Structures*. Youtube Video. Accessed on 2025-02-07.

[8] M. Danielsson. *Modeling the Differential Quenching of a Katana*. Comsol Blog, 2024.

[9] C. Delprete. *Crankshaft*. Slides of the Course Powertrain Components Design, Politecnico di Torino, 2024.

[10] K. Djellabi and M. E. H. Latreche. *Induction Heating Process Design Using Comsol® Multiphysics Software Version 4.2a*. International Journal of Electrical, Electronic and Communication Sciences, 7(1), 2014.

[11] C. Hakan Gür and Caner Simsir. *Simulation of Quenching: A Review*. Materials Performance and Characterization, 1:104479, 2012.

[12] J. Holmberg et al. *Residual stress state in an induction hardened steel bar determined by synchrotron- and neutron diffraction compared to results from lab-XRD*. Materials Science and Engineering: A, 667:199–207, 2016.

[13] D. Hömberg et al. *Simulation of Multi-Frequency-Induction-Hardening Including Phase Transitions and Mechanical Effects*. Finite Elements in Analysis and Design, 121:86–100, 2016.

[14] D. P. Koistinen and R. E. Marburger. *A General Equation Prescribing the Extent of the Austenite–Martensite Transformation in Pure Iron–Carbon Alloys and Plain Carbon Steels*. Acta Metallurgica, 7(1):59–60, 1959.

[15] J. B. Leblond, G. Mottet, J. Devaux, and J. C. Devaux. *Mathematical Models of Anisothermal Phase Transformations in Steels, and Predicted Plastic Behaviour*. Materials Science and Technology, 1(10):815–822, 1985.

[16] P. Mayner, B. Jungmann, and J. Dollet. *Hardenability Concepts with Applications to Steels*. Metallurgical Society of AIME, 1978. ISBN: 9780895201416.

[17] D. Mingardi. *Numerical Models for Induction Hardening of Gears*. Master's thesis, Università degli Studi di Padova, 2012.

[18] V. Nemkov, R. Goldstein, J. Jackowski, et al. *Stress and Distortion Evolution During Induction Case Hardening of Tube*. Journal of Materials Engineering and Performance, 22:1826–1832, 2013.

[19] V. I. Rudnev and D. Loveless. *Comprehensive Materials Processing, 12.15 – Induction Hardening: Technology, Process Design, and Computer Modeling*. Elsevier, 2014. ISBN: 9780080965338.

[20] K. Sadeghipour, J. Dopkin, and K. Li. *A Computer Aided Finite Element/Experimental Analysis of Induction Heating Process of Steel*. Computers in Industry, 28(3):195–205, 1995.

[21] A. Samuel and K. N. Prabhu. *Residual Stress and Distortion During Quench Hardening of Steels: a Review*. Journal of Materials Engineering and Performance, 31:5161–5188, 2022.

[22] M. Selin and K. Furuberget. *Härdning och Materialteknik på Scania*, 2019. Scania.

[23] K. E. Thelning. *Steel and Its Heat Treatment – a Handbook*. Swerea IVF, 2012. ISBN: 9789186401115.

[24] D. Tong et al. *Numerical Simulation of Induction Hardening of a Cylindrical Part Based on Multi-Physics Coupling*. Modelling Simul. Mater. Sci. Eng., 25:035009, 2017.

[25] D. Tong et al. *Numerical Simulation on Induction Heat Treatment Process of a Shaft Part: Involving Induction Hardening and Tempering*. Journal of Materials Processing Technology, 262:277–289, 2018.